Bioactive Materials 47 (2025) 229–247

Contents lists available at ScienceDirect

Bioactive Materials

journal homepage: www.keaipublishing.com/en/journals/bioactive-materials

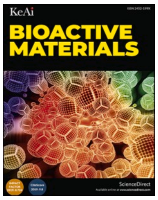

CD9-enriched extracellular vesicles from chemically reprogrammed basal progenitors of salivary glands mitigate salivary gland fibrosis

Sunyoung Park [a,b,1], Yeo-Jun Yoon [c,1], Yongpyo Hong [c,2], Jianning Yu [a,d,2], Jae-Min Cho [c], Ye Jin Jeong [c], Haeun Yu [a], Hyorim Jeong [b], Hyunjin Lee [b], Seungyeon Hwang [c], Won-Gun Koh [e], Ji Yeong Yang [a,b], Kyung-A Hyun [a,f], Hyo-Il Jung [a,b,*], Jae-Yol Lim [c,**]

[a] School of Mechanical Engineering, Yonsei University, 50 Yonsei-ro, Seoul, 03722, Republic of Korea
[b] The DABOM Inc., 50 Yonsei-ro, Seoul, 03722, Republic of Korea
[c] Department of Otorhinolaryngology, Yonsei University College of Medicine, Seoul, 03722, Republic of Korea
[d] Department of Biomedical Laboratory Science, Yonsei University, 1 Yeonsedae-gil, Wonju, Gangwon-do, 26493, Republic of Korea
[e] Department of Chemical and Biomolecular Engineering, Yonsei University, 50 Yonsei-ro, Seoul, 03722, Republic of Korea
[f] Korea Electronics Technology Institute (KETI), Seongnam, Gyeonggi-do, 13509, Republic of Korea

ARTICLE INFO

Keywords:
Extracellular vesicle
Salivary gland
Regeneration
Fibrosis
Organoid
Microfluidics

ABSTRACT

Extracellular vesicles (EVs) derived from stem cells offer promising potential for cell-free therapy. However, refining their cargo for precise disease targeting and delivery remains challenging. This study employed chemical reprogramming via dual inhibition of transforming growth factor beta (TGFβ) and bone morphogenetic protein (BMP) to expand salivary gland basal progenitor cells (sgBPCs). CD9-enriched ($CD9^+$) EVs were then isolated from the sgBPC secretome concentrate using a dual microfluidic chip. Notably, $CD9^+$ EVs demonstrated superior uptake by salivary epithelial cells compared to CD9-depleted ($CD9^-$) EVs and total EVs. *In vivo* studies using a salivary gland (SG) obstruction mouse model and *ex vivo* studies in SG fibrosis organoids revealed that $CD9^+$ EVs significantly enhanced anti-fibrotic effects over $CD9^-$ EVs and control treatments. The presence of miR-3162 and miR-1290 in $CD9^+$ EVs supported their anti-fibrotic properties by downregulating ACVR1 expression. The chemical reprogramming culture method effectively expanded sgBPCs, enabling consistent and scalable EV production. Utilizing microfluidic chip-isolated $CD9^+$ EVs and ductal delivery presents a targeted and efficient approach for anti-fibrotic SG regeneration.

1. Introduction

Despite extensive research and clinical trials [1–8], there are currently no effective treatments available to alleviate salivary gland (SG) fibrosis [9]. Stem cell therapy has been explored as a potential solution due to its anti-inflammatory, anti-fibrotic, and regenerative attributes [10–16]. However, the risks of uncontrolled differentiation and immune rejection have hindered its widespread application [17–21]. An emerging alternative that is gaining prominence is cell-free therapy, especially involving extracellular vesicles (EVs) [22,23]. Recent studies have shown that EVs have comparable therapeutic potential to whole-cell transplants [24–27]. Furthermore, EVs provide regenerative effects without the associated risks of uncontrolled cell behavior and immunogenicity [28]. These EVs present a promising avenue for therapeutic advancement by retaining the therapeutic signaling of stem cells and offering the potential for targeted therapy [29–32]. Additionally, the engineering capabilities of EVs for carrying specific therapeutic cargo enhance precision in treatment, and their engineering is more convenient compared to whole cells [33]. Despite the growing evidence of tissue-resident stem/progenitor cell-derived EVs on tissue regeneration, there are still significant challenges in their clinical application [34,35].

First, standardized purification protocols and scalable production of EVs are prerequisites to establish clinical feasibility [22,35]. The

---

* Corresponding author. School of Mechanical Engineering, Yonsei University, 50 Yonsei-ro, Seoul, 03722, Republic of Korea.
** Corresponding author. Department of Otorhinolaryngology, Yonsei University College of Medicine, Seoul, Republic of Korea.
E-mail addresses: uridle7@yonsei.ac.kr (H.-I. Jung), jylimmd@yuhs.ac (J.-Y. Lim).

[1] The authors contributed equally to this work as co-first authors.

[2] These authors contributed equally to this work as co-second authors.

https://doi.org/10.1016/j.bioactmat.2025.01.019
Received 10 April 2024; Received in revised form 7 December 2024; Accepted 16 January 2025

stability of EVs during storage for clinical utilization needs to be addressed [36]. Second, the safety and efficacy of EVs must be thoroughly evaluated to mitigate concerns regarding systemic effects and the optimal dosage, particularly concerning delivery routes. To tackle these challenges, this study employed innovative approaches. These included reprogramming culture to uniformly expand salivary gland basal progenitor cells (sgBPCs), thereby ensuring consistent production of therapeutic EVs. Furthermore, a microfluidic chip was utilized to selectively enrich a specific population of EVs, enhancing their purity and efficacy [37]. Finally, direct administration of EVs through the retroductal route was employed, enabling targeted treatment with reduced invasiveness and safety concerns. These strategies represent important advancements in overcoming the obstacles associated with EV-based therapies and pave the way for their clinical translation.

CD9 plays a significant role in various biological processes due to its association with membrane dynamics and cellular interactions [38]. It is involved in facilitating membrane curvature and fusion, particularly in areas of high curvature, which is crucial during EV exocytosis. This role in membrane dynamics is critical for the proper release of EVs from cells. Additionally, CD9 contributes to the adhesion and fusion processes during EV endocytosis, which allows EVs to merge with the target cell membrane and deliver their cargo effectively. CD9 is distinct from other tetraspanins, such as CD63 and CD81, due to its prominent role in cell adhesion and binding [39]. This specificity has been highlighted in various studies that explore CD9's involvement in critical processes such as cell migration, fusion, signaling, oocyte-sperm fusion, and even pathological conditions, including cell adhesion during virus infection, glomerular disease progression, and cancer metastasis [40,41].

The study aims to chemically reprogram sgBPCs through transforming growth factor beta (TGFβ) and bone morphogenetic protein (BMP) inhibition, expanding cell populations for therapeutic applications. This reprogramming approach creates a robust population of sgBPCs, which can be utilized in regenerative medicine, particularly for treating SG fibrosis. Additionally, a microfluidic chip-based isolation method is employed to select and enrich CD9$^+$ EVs from the sgBPC secretome concentrate, ensuring high purity and effectiveness of the EVs for therapy. Finally, the study demonstrates that CD9$^+$ EVs derived from reprogrammed sgBPCs significantly improve efficacy in alleviating SG fibrosis, showing notable therapeutic effects within 7 days of administration. These findings highlight the potential of precise EV isolation and reprogramming techniques in advancing EV-based therapies for SG disorders (Fig. S1).

2. Materials and methods

2.1. Human parotid gland epithelial stem cell culture and characterization of the cells

The tissue used for isolating human sgBPCs was obtained from three female donors of parotid glands: a 48-year-old (hPG-106), a 74-year-old (hPG-91), and a 31-year-old (hPG-109). The tissues were cut into small pieces using a razor blade and then digested with collagenase II (Thermo Fisher Scientific, USA) for 1 h. Cells were dissociated by incubation with TrypLE Express Enzyme (Thermo Fisher Scientific, USA) for 10 min at 37 °C with occasional shaking to ensure complete dissociation into a single-cell suspension. The cell suspension was then filtered using a 70 μm cell strainer to remove undigested tissue fragments. The filtered cells were cultured in Dermacult keratinocyte expansion medium (STEMCELL™ TECHNOLOGIES, Canada) supplemented with 10 μM Y27632 (Tocris, UK), a ROCK 1/2 inhibitor; 1 μM A83-01 (Tocris, UK), a TGFβ receptor inhibitor; and 0.1 μM LDN193189 (Tocris, USA), a BMP signaling inhibitor. The culture was maintained in a humidified 5 % CO2 atmosphere at 37 °C. The combination and concentration of small molecules (Y27632, A83-01, LDN193189) were optimized based on prior literature [42,43] and through our experimental adjustments. These molecules were chosen for their roles in maintaining stemness and enhancing the proliferation of sgBPCs while preventing differentiation during early culture. Y27632 helps in survival and proliferation of epithelial cells by inhibiting anoikis, A83-01 blocks differentiation signals and epithelial-mesenchymal transition, and LDN193189 promotes cell growth and prevents premature differentiation into non-epithelial lineages. This specific cocktail of small molecules was added fresh with each medium change every 2–3 days.

The sgBPCs exhibited stem cell properties such as a high population-doubling time across passages, differentiation capacity into SG epithelial cells, and sphere-forming ability, as described in the results. To ensure consistency and reproducibility of the results, sgBPCs at passages three through nine were used in all experiments. To calculate the cumulative population doubling level, dissociated cells were plated in 24-well plates (SPL, Republic of Korea) and maintained at 37 °C in a humidified incubator containing 5 % CO2. Upon reaching 80 % confluence, cells were detached using TrypLE Express Enzyme (Thermo Fisher Scientific, USA) and subsequently passaged until they reached a population doubling level (PDL) of 50. The cumulative PDL was calculated using the formula: $T \times \log(2)/(\log(q2) - \log(q1))$, where T represents the culture duration, q1 is the initial cell number, and q2 is the final cell number. For cell quantification, cells were stained with 0.4 % trypan blue, and viable cells were counted using a Countess II FL (Thermo Fisher Scientific, USA).

2.2. Single cell transcriptome analysis

We imported the output files from our previous data into the Seurat package (v. 4.01) using the read 10X function to obtain single-cell transcriptome data in Seurat format. Based on the principal component analysis (PCA) results, the Uniform manifold approximation and projection (UMAP) method was used for dimensionality reduction and visualization. Different cell types were identified based on previously reported marker genes. A total of 655 cells from the human parotid gland were used for the differential expression analysis.

2.3. Isolation of EVs from sgBPCs

sgBPCs were seeded in a T75 flask with approximately 26,000 cells/cm^2 in DermaCult keratinocyte expansion medium under small-molecule combination conditions. To address the removal of potential influence of the stimulating chemicals, the cells were washed extensively to remove any residual chemicals. The washing procedure involved multiple rounds of centrifugation and resuspension in an appropriate buffer solution to ensure thorough removal of the stimulating chemicals. The culture supernatants for isolation of the EVs were collected after 48 h and centrifuged at 500×*g* for 5 min at 4 °C to remove the cells. Then, the supernatants were centrifuged at 2000×*g* for 30 min and filtered through a 0.22-μm vacuum filter bottle system (Corning, USA) to eliminate large non-EVs, including cell debris, microvesicles, and apoptotic bodies. The EVs from sgBPCs were enriched by tangential flow filtration (Pall Life Science, USA), with 100-kDa molecular weight cutoff filters, for the mass production of EVs. The EVs derived from sgBPCs adhered to the MISEV guidelines for EV isolation, allowing for the assessment of their biophysical characteristics and protein biomarkers, employing non-conditioned medium samples as negative controls [44].

2.4. Microfluidic chip for the enrichment of CD9$^+$EVs

Specific EVs were successfully enriched using a previously reported method [45,46]. The prepared EV sample and solution of anti-CD9 antibody-conjugated microbeads (TheDABOM, Korea) were injected into a microfluidic chip consisting of 150 cycles of horseshoe-shaped channels to enhance the binding between the sgBPC-derived EVs and the antibody-conjugated microbeads. This design maximizes the surface area and retention time of EVs within the channels, promoting higher capture efficiency. The efficiency of candidate CD9 antibodies was validated, and the high Kd value of the antibody was selected in this study (data not shown). The microfluidic chip was placed into a precision syringe pump to control the flow rate. The pre-cleared medium was then passed through the microfluidic chip at a flow rate of 100 μL/min. During this process, a continuous flow of buffer was maintained to wash away unbound particles, ensuring that only CD9^{+} EVs remained associated with the microbeads. The association of CD9^{+} EVs with the microbeads was performed within 10 min for EVs from cell culture medium. Subsequently, the CD9^{+} EVs carrying microbeads were captured in a fish-trap-shaped channel, and the EVs were harvested in an intact form using an elution buffer, which can recover the intact EVs from the beads (TheDABOM, Korea) [45,47]. All the negative controls of the EVs for the further cell analysis were used with eluted media from the beads conjugated with CD9 antibody to identify whether the effect of EVs is affected by the beads or elution buffers (TheDABOM, Korea). The isolated EVs by elution buffer were exchanged with dialysis system into the PBS for the further study.

2.5. Nanoparticle tracking analysis (NTA) of EVs

NTA was used to characterize the stability for the EVs using a nanoparticle tracking analysis system (Malvern Panalytical, UK) equipped with a 642-nm laser and NTA software (NanoSight, USA). The analysis was performed at 22 °C with a gain of 16 and a frame rate of 30 frames per second. Image evaluation was performed by measuring the particles for 10 s in triplicate.

2.6. Transmission electron microscopy (TEM) of EVs

We dropped 10 μL of the EV solution and dried it on a copper grid with 200 mesh carbon films (Electron Microscopy Sciences, USA). It was then washed with three drops of PBS and distilled water. Subsequently, a drop of UranyLess EM staining solution (EMS, Belgium) was incubated on the grid for 3 min to induce negative EV staining. After washing thrice with distilled water, the excess solution was drained with a filter paper. The grid with the sections was dried at room temperature (RT). The EV structures were observed using a JEM-2100plus (JEOL, USA).

2.7. Flow cytometry analysis of cells and EVs

For identification of the isolated epithelial cells, the sgBPCs were trypsinized to a single-cell suspension. After harvesting, the cells were subjected to Fc blocking by incubation with human Fc receptor-binding inhibitor (Thermo Fisher Scientific, USA) for 10 min at 4 °C to prevent non-specific binding of antibodies. Various antibodies targeting stem cell markers, vascular markers, and mesenchymal markers were diluted in FACS buffer (PBS containing 1 % BSA and 0.1 % NaN3) and incubated in the dark at 4 °C for 30 min. Isotype controls were also prepared for each antibody (Table S1). For EVs, the CD9, CD81, and CD63 surface proteins on the CD9^{+} EV-captured microbeads and sgBPCs were measured via flow cytometry to profile the proteins on the surface membranes. CD9, CD81, and CD63 are well-established tetraspanins commonly used in EV research to identify and characterize EVs [44]. The captured CD9^{+} EVs were washed in ice-cold FACS buffer. The fluorescent primary antibodies were each incubated for 30 min at 4 °C in the dark. The captured CD9^{+} EVs and sgBPCs were rinsed with FACS buffer three times to remove non-specific binding, and then analyzed using a FACS LSR II flow cytometer (BD Biosciences, USA). See Table S1 for detailed antibody information.

2.8. Western blot of EVs

Cell lysates (CL) for western blotting were obtained by incubating cell pellets with a concentration of 10^{6} cells in 25 μL of RIPA buffer (Thermo Fisher Scientific, USA) and EV precipitates in resuspension buffer for 20 min on ice. The cell pellets were then centrifuged at 13,000×g for 15 min at 4 °C to recover the supernatant. EVs were isolated using a resuspension buffer to isolate protein (Thermo Fisher Scientific, USA). To ensure accuracy in our protein quantification and comparisons, we loaded an equal amount of protein (20 μg) for each sample. The samples were mixed with 4X loading buffer (Thermo Fisher Scientific, USA) without a reducing agent. After incubation for 10 min at 70 °C, the samples were loaded on sodium dodecyl sulfate-polyacrylamide gel electrophoresis (SDS–PAGE) gel. To prevent non-specific binding of the primary antibodies, a blocking step was performed for 30 min using a blocking buffer (Sigma-Aldrich, USA), and primary antibodies were incubated overnight at 4 °C and secondary antibodies for 2 h at 25 °C. Development was performed using Clarity Western ECL Substrate (Bio-Rad, USA) and iBright 1500 imager (Thermo Fisher Scientific, USA). The intensities of the bands were quantified using ImageJ software.

2.9. Mass spectrometry analysis of EVs

LC-MS/MS was performed using a UPLC-Orbitrap Explores 480 mass spectrometer for three replicates of each of the three samples (total EVs, CD9^{+} EVs, and CD9^{-} EVs) from sgBPC EVs. The proteomic analysis identified a wide range of proteins, including those involved in cellular communication and signaling, which may reflect the functional roles of the EVs in sgBPC biology. Comparative analysis between CD9^{+} EVs and CD9^{-} EVs revealed distinct protein profiles, suggesting functional differences between these EV subpopulations. All samples were pretreated through filter aided sample preparation (FASP) digestion with a fixed protein amount of 100 μg according to the manufacturer's protocol. The pretreated peptides were desalted using a C18 microspin column. After that, 100 % methanol, 0.1 % formic acid, 80 % ACN, and 0.1 % formic acid were sequentially added, and the sample was loaded. Then, 0.1 % formic acid was added to remove unnecessary materials, and 80 % ACN was added to elute the peptides. Peptide separation was performed at a flow rate of 300 nL/min using a 50 cm × 75 μm C18 column (PepMapTM RSLC, 2 μm, 100 Å). To identify the analytes, data were searched against the Homo sapiens (UP000005640) UniProt database using Sequest-HT in Proteome Discoverer (version 2.4).

2.10. Differential expression and gene ontology analyses of EVs

Normalization and differential expression analyses of CD9^{+} EVs and CD9^{-} EVs compared to total EVs were performed by using the ClustVis package. p-values were calculated and corrected for multiple testing using the Benjamini–Hochberg method. Sample clustering and PCA were performed using pheatmap and ggplot2, respectively. Gene ontology (GO) analysis was conducted to classify the associated mechanisms into three categories: biological processes (BP), cellular components (CC), and molecular functions (MF). This analysis revealed key biological pathways and molecular functions that were enriched in the different EV subpopulations, providing insights into their potential roles in sgBPC biology and disease mechanisms. The lists relevant to interactional genes from significant GO terms (p-value <0.05) were identified by the FunRich software and STRING using the proteome database.

2.11. RNA library preparation and sequencing of EVs

Total RNAs from different EV groups (Total EVs, CD9^{+} EVs, and CD9^{-} EVs) derived from sgBPCs EVs were isolated by using TRIzol Reagent (Thermo Fisher Scientific, USA) according to the manufacturer's instructions. The RNA quality and quantity were assessed using a NanoDrop 2000 spectrophotometer (Thermo Fisher Scientific, USA). Subsequently, short-chain RNAs (miRNA) libraries were prepared using the NEBNext Multiplex Small RNA Library Prep Set for Illumina® (NEB, USA). miRNA sequencing provided a detailed profile of the small RNA content within the EVs, revealing specific miRNAs that are differentially packaged into CD9$^+$ EVs and CD9$^-$ EVs. These miRNAs may play crucial roles in the EV-mediated regulation of target cells and were further analyzed for their involvement in relevant signaling pathways using bioinformatic tools. miRNA sequencing was performed using the NextSeq500 platform (Illumina, USA) with single-ended 75 bp sequences. The BAM file (alignment file) was obtained by mapping sequence reads using Bowtie2 software tool. Mature miRNA sequences were used as reference sequences for mapping. The read counts mapped to mature miRNA sequences were extracted from the alignment file using Bioconductor, which uses R version 3.2.2 and bed tools version 2.25.0. The read counts of the annotated miRNAs were normalized using the trimmed mean of m-values (TMM) and counts per million (CPM) methods for comparison between samples. To identify differentially expressed miRNAs between CD9$^-$ EVs and CD9$^+$ EVs, a volcano plot analysis was performed. This analysis highlighted miRNAs that were significantly upregulated or downregulated in CD9$^+$ EVs compared to CD9$^-$ EVs, using fold-change thresholds and adjusted *p*-values to determine significance. The volcano plot provided a clear visual representation of the miRNAs that are selectively enriched in either EV population, offering insights into their potential functional roles.

2.12. EV uptake assay

To identify the effect of the uptake of EVs, primary salivary epithelial cells were seeded at a density of 10^4 cells per well on an 8-well culture slide and then incubated at 37 °C. After 24 h of incubation, the cells were supplemented with PBS, total EVs, CD9$^-$ EVs, and CD9$^+$ EVs, at a density of 10^7 particles per well. After 4 h, each well was washed with PBS and fixed in a 4 % PFA solution. DAPI (Thermo Fisher, USA) was used to stain the nuclei, and EVs internalization was evaluated using a confocal microscope LSM980 (Carl Zeiss, Germany). The organoid EV uptake assay was performed on organoids cultured on chamber slides with 500 cells seeded per well and cultured for 6 days. Total EVs at a concentration of 10^7 particles/mL were added to the culture medium. After 30 min, 2 h, 4 h, and 24 h, the culture medium was removed, and the organoids were rinsed with PBS. They were then fixed with 2 % paraformaldehyde and 0.1 % glutaraldehyde at room temperature for 30 min. Subsequently, permeabilization was carried out using PBS containing 0.1 % Tween-20 for 30 min, followed by washing with PBS. The organoids were stained with Alexa Fluor 488 Phalloidin (Thermo Fisher, USA) to visualize F-actin for 1 h, followed by washing with PBS. Counterstaining was performed using DAPI, and images were acquired using an LSM980 confocal microscope. All samples were imaged under identical conditions, including exposure time, light intensity, and magnification, to ensure consistency across different groups.

2.13. Immunofluorescence

The SGs and organoid were fixed with 10 % neutral buffer formalin (10 % NBF). The tissues were dehydrated and embedded in paraffin. Paraffin sections (5 μm thick) were dewaxed using xylene. According to standard procedures, sections were boiled in Tris-EDTA buffer (pH 9.0) for 40 min for antigen retrieval. After antigen retrieval, the section was incubated with 5 % normal donkey serum for 1 h at 25 °C to block non-specific antigen-binding sites. Then, the sections were incubated with primary antibodies overnight at 4 °C. The sections were then washed in tris-buffered saline (TBS) and incubated with the corresponding secondary antibodies conjugated to Alexa Fluor (Thermo Fisher Scientific, USA) for 60 min at 25 °C in the dark. They were then washed in TBS, treated with DAPI, cover slipped with mounting medium, and examined under an LSM 700 (Carl Zeiss, Germany) or ECLIPSE Ti2 (Nikon) microscope. Quantification of multiplex-stained tissues was performed using ImageJ software (National Institutes of Health) as follows. The loaded image files were separated by color channels, and thresholds were set to extract only the stained regions. Subsequently, the number or area of fluorescently stained cells was measured using the "measure particles" option. When counting cells, the circularity option in "measure particles" was set to a value of 0.5–1.0, and when measuring the area, it was set to 0–1.0. For markers such as Ki67, which are not abundantly present, manual counting was performed. Please see Table S1 for detailed antibody information.

2.14. Tissue histology

The fixed tissues were embedded in paraffin, sectioned, deparaffinized, and rehydrated. Sections were stained with hematoxylin and eosin (H&E, Abcam, UK) for histological examination, as well as Masson's trichrome (MTC, Abcam), periodic acid–Schiff (PAS, Abcam), and Picro Sirius red (Abcam) staining, according to the manufacturer's instructions. Two blinded examiners assessed pathological changes, including inflammation and structural damage (H&E), mucosubstance including mucin components (PAS), total fibrosis (MTC), and collagen I/III (Sirius Red). Masson's Trichrome (MTC) staining was used to visualize collagen deposition within the overall tissue architecture, providing an overview of fibrosis and its structural integration. Sirius Red staining highlighted collagen density and composition, allowing for a more detailed assessment of fibrotic changes. SG damage scores (H&E) were assigned on a scale of 0–5, based on the following criteria: intact acini in image fields were scored as 0 for 90 % or more, 1 for 70%–90 %, 2 for 50%–70 %, 3 for 30%–50 %, 4 for 10%–30 %, and 5 for 10 % or fewer intact acini. This scoring method has been consistently applied in previous studies conducted by our group [10,48–50]. The mucosubstance area, including mucin, and the fibrosis levels were measured as area ratios, with magenta for PAS, blue for MTC, and red for Sirius red staining.

2.15. Quantitative real-time PCR (RT-qPCR)

Total RNA was extracted using the TRIzol Reagent (Thermo Fisher Scientific, USA). Moreover, 500 ng of total RNA was subjected to first-strand complementary DNA (cDNA) synthesis (Takara Bio, Japan). The glyceraldehyde-phosphate dehydrogenase gene was used as an internal control to normalize sample differences. Real-time PCR was performed using the SYBR Green Lo-ROX qPCR kit (Bioline, USA) and QuantStudio™ 5 System (Thermo Fisher Scientific, USA). Micro RNA expression was determined using TaqMan microRNA assay kits (Thermo Fisher Scientific, USA), with U6 as a reference. Sample quantification for miRNA and mRNA was performed according to the threshold cycle using the ΔΔCt method. The values presented in the graphs represent the mean ± SD. See Table S2 for detailed primer sequences and information.

2.16. Target prediction of significant miRNAs

Normalization and differential expression analysis between CD9$^+$ EVs and CD9$^-$ EVs derived from sgBPC EVs were performed by using the DEseq2 package. *p*-values were calculated and corrected for multiple testing using the Benjamini–Hochberg method. Normalized expression volcano plots were generated using the ggplot2 R package. Based on the differentially expressed miRNAs, target mRNA in CD9$^+$ EVs were obtained using the following steps. Targetscan (http://www.targetscan.org/), miR-DB (http://www.mirdb.org/), and miRTarBase (http://mirtarbase.mbc.nctu.edu.tw/) were used to obtain potential target mRNAs, which were further filtered by Pearson correlation coefficient (PCC) analysis between the expression levels of mRNA and miRNA in CD9$^+$ EVs ($\text{PCC} < -0.3$ and $p < 0.05$). The KEGG pathway and its associated target genes from the predicted mRNAs were used to classify the associated mechanisms of CD9$^+$ EVs.

2.17. Plasmids and dual-luciferase reporter assay

To identify the direct targets of miR-4443, miR-3162, and miR-1290, wild-type and mutant ACVR1 mRNA were amplified and inserted into the pmirGLO Dual-Luciferase miRNA Target Expression Vector (Promega, USA) between the PmeI and XbaI restriction sites. All recombinant vectors were verified using Sanger sequencing (Cosmo Genetech, Korea). For the dual-luciferase reporter assay, cells were lysed and processed for 24 h before the contents were collected. The luciferase activities of Firefly and Renilla were detected using the Dual-Luciferase® Reporter Assay System (Promega), and the relative luciferase activity of each sample was determined using the Firefly/Renilla ratio.

2.18. SG organoid culture and activin A-induced fibrosis modeling

Human parotid gland-derived organoids were cultured and maintained by previously reported method [51]. Organoids were used as a model system to evaluate the efficacy of these EVs. On the sixth day after the organoids were cultured, Y27632 was removed from the basal medium, and 20 ng/mL of Activin A (Peprotech, USA) and 10^7 particles of $CD9^-$ EVs or $CD9^+$ EVs were added. Organoids cultured for an additional 2 days were harvested and analyzed for histology and transcript changes. Cell viability of organoids was measured using CellTiter-Glo® 3D product (Promega, USA). The results are presented as the mean ± standard deviation of three biological replicates.

2.19. Mice ductal obstruction modeling

Female C57BL/6 mice (19–21 g) were purchased from Orient Bio, Korea. The mice used in this study were 8-week-old females. The mice were provided a standard pelleted diet and water ad libitum and housed under a 12-h light/dark cycle. They were randomly assigned to the following groups: (1) sham group, which only received an incision; (2) PBS group, which underwent de-ligation 2 weeks after ligation and was administered PBS; (3) $CD9^-$ EVs group, which underwent de-ligation 2 weeks after ligation and was administered $CD9^-$ EVs; and (4) $CD9^+$ EVs group, which underwent de-ligation 2 weeks after ligation and was administered $CD9^+$ EVs. A total of 44 mice were used in the study to ensure robust statistical analysis and reproducibility. The sham group included four mice, the PBS group included nine mice, and the $CD9^-$ EV and $CD9^+$ EV treatment groups each included eight mice. To assess the efficacy of long-term frozen EVs, three mice were used per group.

Prior to submandibular duct ligation, the mice were anesthetized with an intraperitoneal injection of ketamine® (100 mg/kg, Yuhan Corporation, Seoul, Korea) and Rompun® (10 mg/kg, Bayer HealthCare, Mississauga, Ontario, Canada) at a 1:1 ratio. After sterilizing the head and neck with povidone-iodine, a 1–2 cm incision was made to expose the main excretory ducts of the submandibular glands (SMGs). The left SMG duct was ligated approximately 3 mm distal to the gland using a sterile 6-0 silk suture, and the incision was closed with a 3-0 black silk suture. The experimental design was based on existing models, including our previous studies [14,15]. While de-ligation is typically performed within 7 days to prevent irreversible damage, we extended the ligation period to 14 days to induce partially irreversible damage. After 14 days, the ducts were deligated by removing the silk suture. Following de-ligation, either $CD9^+$ EVs or $CD9^-$ EVs (10^9 EV particles/20 μL) were injected retroductally at a rate of 20 μL/min for 3 consecutive days. EV administration over 3 days followed a previously established protocol, optimizing EV uptake by the target tissue while minimizing potential side effects associated with multiple injections. The retroductal delivery was performed using a cannula with the following specifications: 11.7 cm in length, 0.010 inches in outer diameter, 0.005 inches in inner diameter, 32G gauge, and manufactured as part of the Intrathecal Catheter System (Braintree Scientific, Catalog #CS-32). The cannula was carefully inserted into the submandibular duct orifice, as previously described [48–50,52].

2.20. SG weight and function evaluation

Seven days after EV administration, the mice were euthanized, and the extirpated SMGs were weighed and compared among the groups. Body weight was measured during the follow-up. Before extirpation, the mice were intraperitoneally administered the muscarinic agonist, pilocarpine (5 mg/kg), to stimulate salivary secretion. Lag time (in seconds) is defined as the period between the injection of pilocarpine and the onset of saliva secretion. This measurement serves as an indirect indicator of the functional recovery or extent of damage to the salivary glands following injury. A shorter lag time reflects better salivary gland function, whereas a longer lag time suggests ongoing damage or incomplete recovery. Saliva was collected from the floor of the mouth using a micropipette, 5 min after stimulation. The collected saliva was placed in pre-weighed microcentrifuge tubes of 1.5 mL, and the salivary flow rate (SFR) (μL/min) was calculated by dividing the total volume (μL) of saliva collected by the collection time (min); the weight of SMGs (mg) was defined as the time from stimulation to the beginning of saliva secretion.

2.21. Statistical analysis

Statistical analysis of KRT5 and KRT7 expression in 2D and 3D cultures was performed using Student's t-test due to its robustness in detecting differences between two groups. Similarly, the mean fluorescence intensity (MFI) of beads bound to fluorescently labelled CD9, CD81, and CD63 EVs was analyzed using Student's t-test compared to control beads. Furthermore, size, concentration, zeta potential, and MFI according to storage time were evaluated using a paired *t*-test. All experiments were performed in triplicate.

For *in vivo* experiments, statistical significance was defined as **p*-value <0.05, ***p* -value <0.01, and ****p* -value <0.001 relative to the sham group, and #*p* -value <0.05, ##*p* -value <0.01, and ###*p* -value <0.001 relative to the PBS group. One-way ANOVA with Tukey's post-hoc test was used for comparisons involving multiple groups such as the sham group, PBS group, $CD9^-$ EVs group, and $CD9^+$ EVs group to control for Type I error in multiple comparisons.

For *ex vivo* organoid experiments, statistical significance was defined as * *p* -value <0.05, ***p* -value <0.01, and ****p* -value <0.001 relative to the untreated group; #*p* -value <0.05, ##*p* -value <0.01, and ###*p* -value <0.001 relative to the Activin A-treated group; $ *p* -value <0.05, $$ *p* -value <0.01, and $$$ *p* -value <0.001 relative to the Activin A with dexamethasone group; and % *p* -value <0.05 relative to the Activin A with $CD9^-$ EVs group. One-way ANOVA with Tukey's post-hoc test was applied to compare the untreated, Activin A-treated, Activin A with dexamethasone-treated, $CD9^-$ EV-treated, and $CD9^+$ EV-treated groups.

Statistical analyses were performed using GraphPad Prism version 8.0.2 (GraphPad Software, California, USA). All experiments were performed in triplicate, with three independent biological replicates ($n = 3$) for each condition. Data variability is presented as mean ± standard deviation (SD).

3. Results

3.1. Chemically reprogrammed SG cells can maintain their epithelial progenitor characteristics even during long-term culture

We established a robust method for cultivating human sgBPCs in a controlled environment, based on a chemical reprogramming of SG cells. The addition of small molecules (ROCK 1/2, TGFβ, and BMP pathway inhibitors) enabled the maintenance of epithelial characteristics and sustained long-term culture (Fig. 1a). The cultured cells underwent more than 50 population doublings and maintained their polygonal morphology for around 60 days (Fig. 1b and c). The cultured cells expressed KRT5, KRT14, KRT19, TP63, and SOX9, key markers consistent with sgBPCs (Fig. 1d). They had limited expression of KRT7 and SOX2, which are markers associated with fully differentiated luminal cells and acinar progenitor cells in adult human SG, respectively. Even after prolonged culture, the epithelial cell marker CDH1

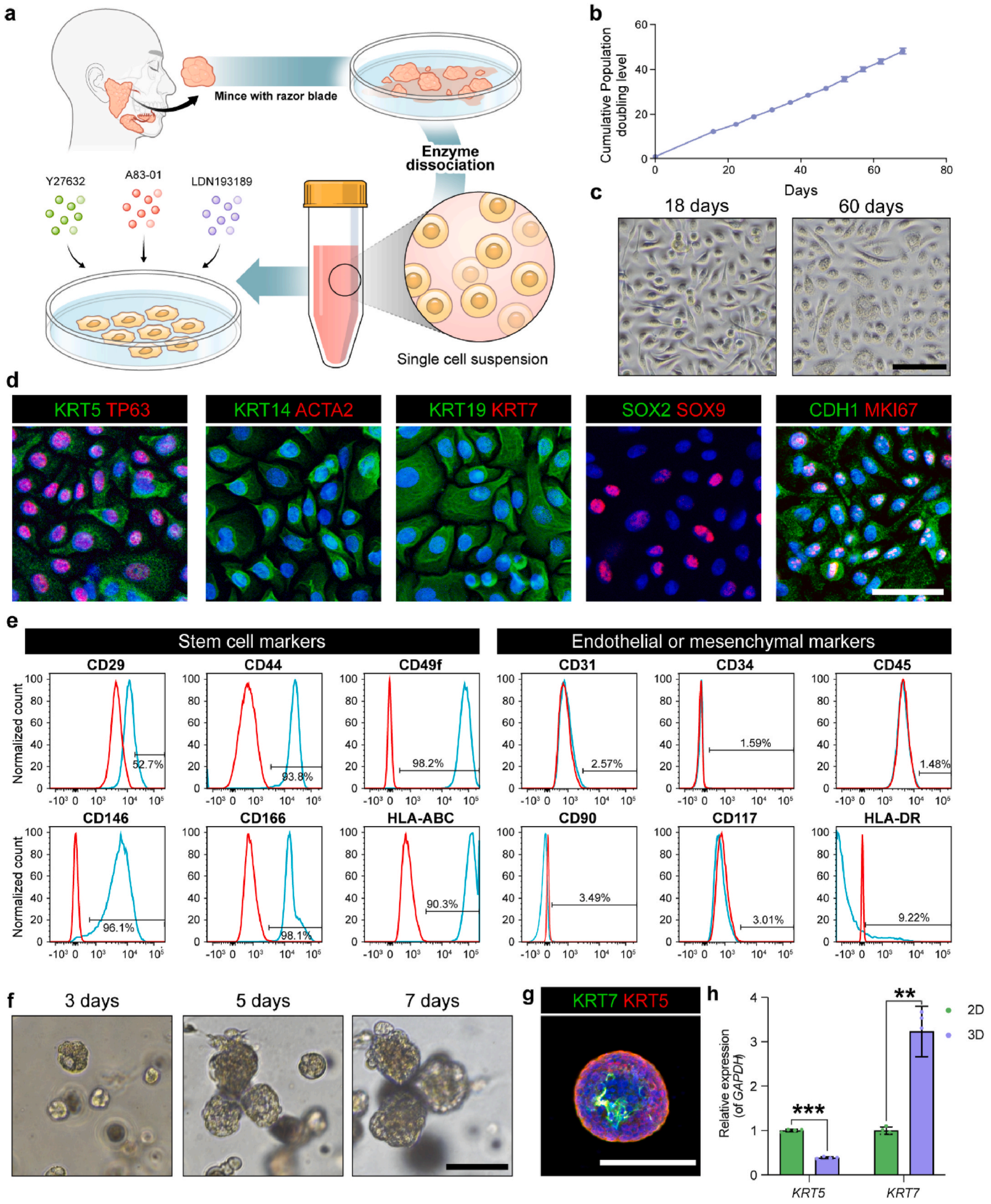

(caption on next page)

Fig. 1. Salivary gland (SG) basal progenitor cells (sgBPCs) isolation and characterization. (a) Schematic representation of sgBPCs isolation from the human parotid gland and culture with small molecule combination Y27632 (Rho-associated protein kinase 1/2 [ROCK] 1/2 inhibitor), A83-01 (transforming growth factor-beta [TGFβ] inhibitor), and LDN193189 (bone morphogenetic protein [BMP] inhibitor). (b) Population doubling graph of sgBPCs under optimal chemical reprogramming cell culture condition. (c) Brightfield microscope images of early (after 18 days of culture) and late passage (after 60 days of culture) sgBPCs. (d) Immunofluorescent (IF) staining of sgBPCs maintained in the chemical reprogramming cell culture condition for basal duct (KRT5; green, TP63; red), basal ductal and/or myoepithelial (KRT14; green, ACTA2; red), ductal progenitor and terminally differentiated luminal (KRT19; green, KRT7; red), acinar progenitor and ductal progenitor (SOX2; green, SOX9; red), proliferating epithelial cells (CDH1; green, MKI67; red) markers. Nuclei were counterstained with DAPI (blue). Scale bar indicates 50 μm. (e) Flow cytometry assessing the expression of various stem cell and endothelial or mesenchymal markers in sgBPCs. (f) Time-lapse images of sgBPCs-induced organoids grown in Matrigel at each time point, with a scale bar indicating 100 μm. (g) IF microscopy of luminal (KRT7; green) and basal (KRT5; red) on 3D cultured for 7 days in sgBPCs. Scale bar indicates 50 μm. (h) RT-qPCR validation for the expressions of *KRT7 and KRT5* between 2D and 3D cultured sgBPCs. Data are representative of at least three independent experiments and are presented as mean ± SD, with **p*-value <0.05. Scale bar indicates 50 μm.

remained prominently expressed, and the expression of MKI67 indicated that cell division actively occurred even after long-term culture [53]. We conducted a study to verify the identity of selectively cultured cells by analyzing a single-cell transcriptome database using the accession code "GSE184526" [51]. Our analysis showed that our culture approach successfully enriched sgBPCs, as indicated by cell type annotation and expression markers (Figs. S2a–c).

Flow cytometry analysis further confirmed that the cultured cells from three different human SG specimens consistently lacked expression of endothelial and mesenchymal markers (CD31, CD34, CD45, CD90, CD117, and HLA-DR) (Fig. 1e and Table S1). Conversely, the presence of markers such as CD29, CD44, CD49f, CD146, CD166, and HLA-ABC, which are associated with SG epithelial or epitheliomesenchymal stem cells, was consistently observed. The characteristics of epitheliomesenchymal markers were identified in human SGs in previous studies [54,55]. The cultured cells were able to form 3D SG structure when cultured in a Matrigel along with a previously reported human SG organoid culture medium (Fig. 1f) [51]. The differentiation potential of sgBPCs was confirmed through analysis of the organoids, which showed an increase in the expression of the terminally differentiated luminal cell marker (*KRT7*) and decrease of basal cell marker (*KRT5*), validated through both immunofluorescence and reverse transcription-quantitative polymerase chain reaction (RT-qPCR) (Fig. 1g and h). In addition, we found through bulk RNA sequencing and gene ontology analysis that combining small molecules for chemical reprogramming increased the secretion and production capacity of exosomes in SG cells (Figs. S2d and e). The volcano plot analysis showed significant differences in gene expression between cells treated with small molecules and those that were untreated (without small molecules) (log2 fold change ≥1.5, *p*-value <0.05). Specifically, 588 differentially expressed mRNAs were identified in cells treated with small molecules compared to untreated cells, with 433 mRNAs being upregulated (red) and 155 mRNAs being downregulated (blue) (Fig. S2d). To explore the functional characteristics of these differentially expressed genes (DEGs), GO terms were analyzed using the FunRich tool. The DEGs were primarily associated with the extracellular space, followed by categories such as secreted, extracellular exosome, MHC class I, extracellular region, MHC class I protein complex, cell surface, intermediate filament, extracellular matrix, and cell junction (Fig. S2e). This result indicates that the presence of small molecules has a notable impact on the expression of certain features, highlighting the potential regulatory effects of these molecules on cellular processes.

3.2. sgBPC-derived EVs enriched with CD9 by the microfluidic chip can remain standardizable and stable specific EVs

Tetraspanins present on the surfaces of EVs are commonly shared with the plasma membranes of the releasing cells. We conducted single-cell RNA sequencing analysis and found that the basal ductal cell subset of SG epithelial cells had high levels of CD9 expression, while CD63 and CD81 were less expressed in these cells but were more prominent in stromal, endothelial, and luminal duct cells (Fig. 2a and Figs. S3a–c). Tetraspanin genes tended to show an increase when cultivating sgBPC, including small molecules (Figs. S3d–f). We assumed that the specific EV population enriched with a tetraspanin might show promise as a potential therapeutic as EVs come "pre-programmed" with specific cargoes and cell-targeting components, prompting various strategies to decipher their tropism and paracrine effects [56,57].

To obtain CD9$^+$ EVs from sgBPCs with higher purity and quality, we developed a microfluidic chip based on affinity-binding principles to selectively isolate CD9$^+$ EVs from the sgBPC secretome concentrate (Fig. 2b). This chip allows for efficient binding of EVs on antibody-coated beads, followed by the isolation of CD9$^+$ EVs within a remarkably short period of 20 min. We successfully validated the enrichment microfluidic system, compared it with conventional affinity-based methods and other isolation systems from previous studies [45,47,58], and obtained the intact specific EVs. We evaluated total EVs, CD9$^-$ EVs, and CD9$^+$ EVs through nanoparticle tracking analysis (NTA) and transmission electron microscopy (TEM), which showed that we successfully isolated CD9$^+$ EVs characterized by intact morphology and a size range of 50–150 nm (Fig. 2c–e). The CD9$^+$ EVs exhibit a much narrower and more uniform size distribution, compared to CD9$^-$ EVs or total EVs. Affinity-based separations using microfluidic chips have enabled high purity and size homogeneity. CD9$^-$ EVs and total EVs, on the other hand, had a greater variation in size due to a mixture of microvesicles and apoptotic bodies [59–62]. This allows CD9$^+$ EVs to deliver more consistent therapeutic efficacy and efficient delivery to target cells. The western blotting technique confirmed that CD9 antibodies had a higher affinity to sgBPCs compared to CD63 and CD81 antibodies, further validating the efficacy of the separation purification chip in isolating CD9$^+$ EVs (Fig. 2f). The results also showed that EVs derived from sgBPCs captured using CD9 displayed bands for CD81, while there were no bands for CD63. This supports the reports that CD9 is usually found co-localizing with CD81 in the same vesicles, while CD63 is often found separately [63]. Mean fluorescence intensity (MFI) analysis revealed that CD9 was significantly enriched on the surface of CD9$^+$ EVs, constituting approximately 58.5 % of the total surface proteins, as opposed to CD81 and CD63 (Fig. 2g–j).

The stability of CD9$^+$ EVs over a long-term storage period at −80 °C was also verified. The size, concentration, and zeta potential (indicative of surface charge) of the EVs remained consistent for a duration of 6 months, indicating the preservation of their physical attributes (Fig. 2k-m). Notably, the EVs maintained a negative zeta potential of −16 mV, implying the retention of phospholipids, such as phosphatidylserine, on their membranes (Fig. 2m). Flow cytometry analysis further substantiated the sustained presence of CD9$^+$ EVs over the storage period, emphasizing the stability of both the EVs' physical properties and molecular characteristics (Fig. 2n). These findings confirm the stability and unique properties of CD9$^+$ EVs isolated through our microfluidic chip-based approach.

3.3. sgBPC-derived EVs enriched with CD9 have better cellular uptake by the interaction of surface proteins

Using liquid chromatography-tandem mass spectrometry (LC-MS/MS), we compared the cargoes in CD9$^+$ EVs with those in total EVs and depleted CD9$^-$ EVs (Fig. 3a). We found a significant difference in the enriched proteins between CD9$^+$ EVs, CD9$^-$ EVs, and total EVs (with a

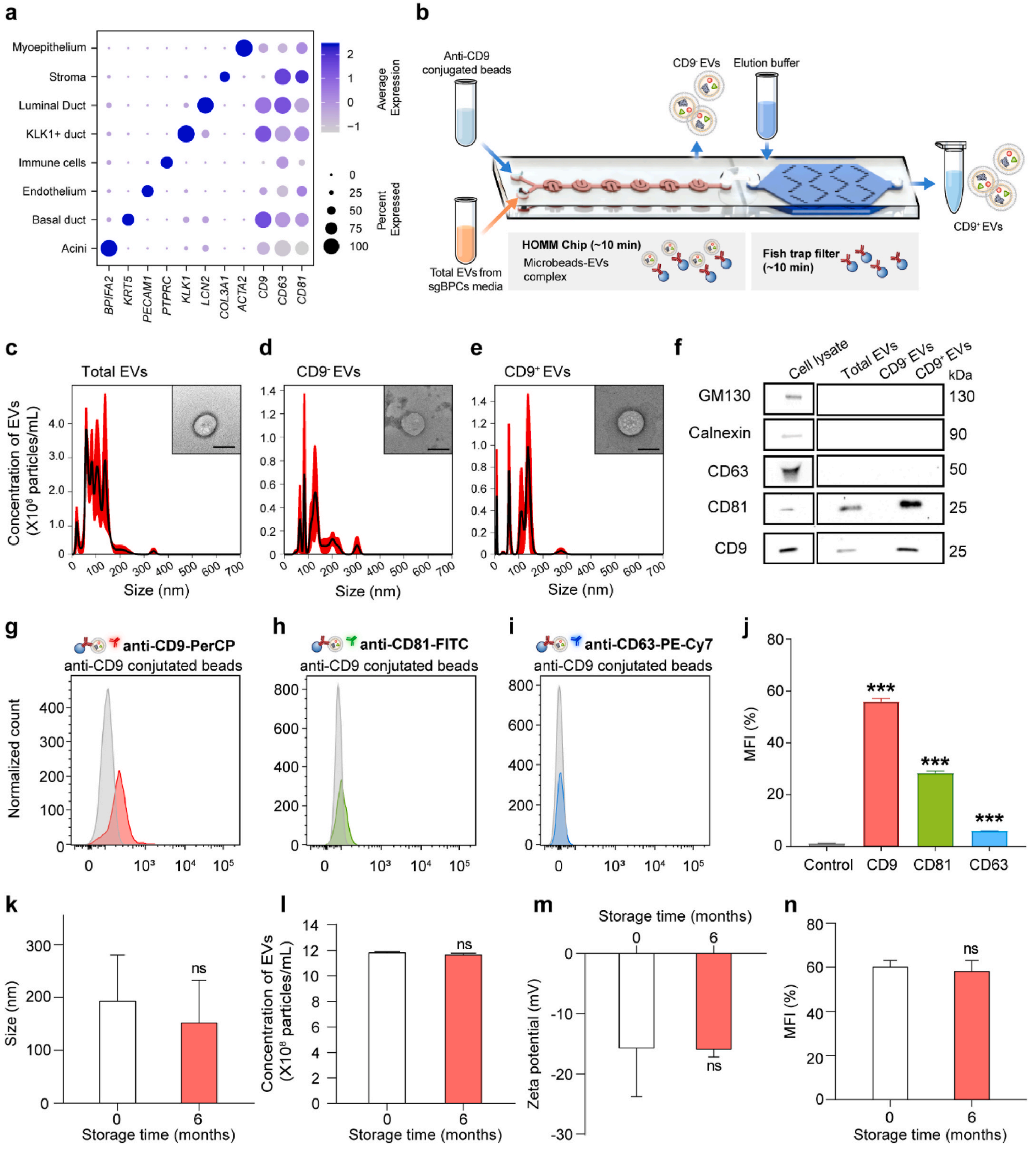

Fig. 2. Isolation and characterization of sgBPCs-derived EVs. (a) Dot plots displaying the cluster-specific representative gene signatures of types of cells with epithelial and exosome markers. (b) Schematic representation of microfluidic device. (c–e) EVs concentration and morphology of total EVs, CD9-depleted EVs ($CD9^-$ EVs), and CD9-enriched EVs ($CD9^+$ EVs) measured by nanoparticle tracking analysis (NTA) and transmission electron microscopy (TEM). (f) Western blotting images of the cell lysate, total EVs, $CD9^-$ EVs, and $CD9^+$ EVs. (g–i) Flow cytometry analysis showing the expression of CD9, CD81, and CD63 on the $CD9^+$ EVs. (j) Bar plot of the expression levels of EV markers (CD9, CD81, and CD63) on the $CD9^+$ EVs. Mean fluorescent intensity (MFI) was analyzed by the normalization of control. (k–n) Bar plot of size, concentration, zeta potential, and MFI of the $CD9^+$ EVs after being stored at −80 °C for 6 months. Scale bar indicates 100 nm.

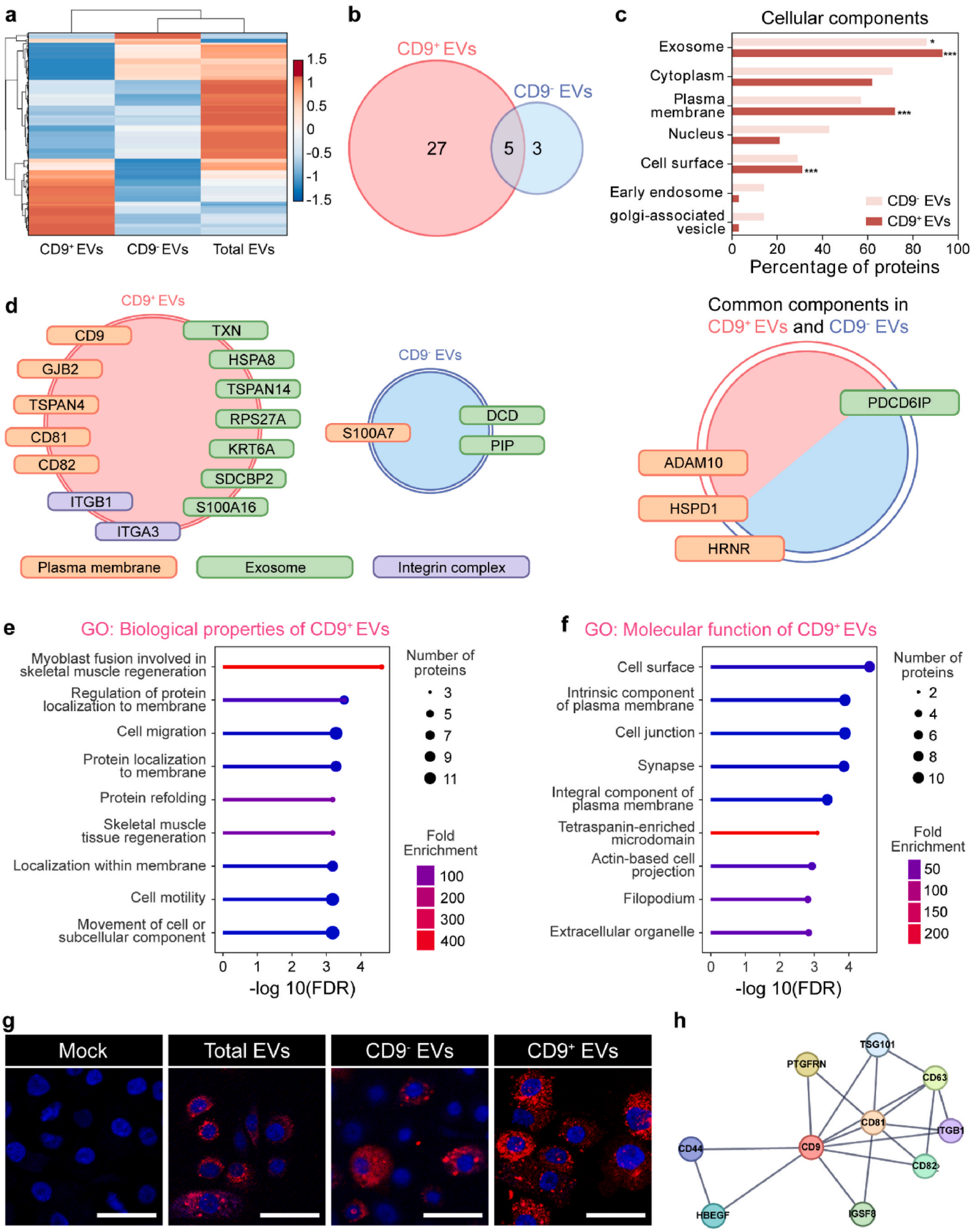

(caption on next page)

Fig. 3. Proteomic analysis of EVs isolated and purified from sgBPCs. (a) Heatmap showing the significant proteins of total EVs, $CD9^-$ EVs, and $CD9^+$ EVs from sgBPCs. High expression of EV proteins is shown in red, while low expression of EV proteins is shown in blue. (b) Venn diagram of numbers of proteins and lists of enriched proteins in $CD9^+$ EVs and $CD9^-$ EVs. (c) Gene enrichment analysis for biological properties category among the proteins enriched in the $CD9^-$ EVs or $CD9^+$ EVs. (d) Schematic representation of the transmembrane proteins identified in the $CD9^+$ EVs and $CD9^-$ EVs, and common proteins identified in the $CD9^+$ EVs and $CD9^-$ EVs. Gene ontology (GO) enrichment analysis of the (e) biological properties and (f) molecular function for $CD9^+$ EVs showing top significant enrichment and number of proteins with the adjusted p-value <0.05. (g) Cellular uptake of total EVs, $CD9^-$ EVs, and $CD9^+$ EVs (EVs stained with Dil; red) in cultured salivary epithelial cells. Nuclei were counterstained with DAPI (blue). (h) Protein-protein interaction networks with CD9. Scale bar indicates 50 μm * p-value <0.05, ***p-value <0.001.

fold change greater than 2) (Tables S3 and S4). The $CD9^+$ EVs contained nine-fold more highly expressed proteins than the $CD9^-$ EVs (Fig. 3b). To understand the differences in subcellular origin of the enriched proteins between $CD9^+$ EVs and $CD9^-$ EVs, we used FunRich software to compare a reference database of over 5000 cellular component proteins with a list of proteins. We calculated the percentages of proteins and significance of each $CD9^+$ EV and $CD9^-$ EV (Fig. 3c). We found that both $CD9^+$ EVs and $CD9^-$ EVs showed significant enrichment of exosomes (93.1 % and 85.7 % of the total proteome, respectively). In particular, $CD9^+$ EVs were significantly enriched in the plasma membrane and cell surface proteins, comprising 72.4 % and 30.2 % of the total proteome, respectively (p-value <0.001) (Fig. 3c–Tables S5 and S6). These surface proteins from $CD9^+$ EVs help in the paracrine effect and increase cell-to-cell communication [56].

The enriched proteins of $CD9^+$ EVs showed plasma membrane proteins such as GJB2, CD9 and, TSPAN4, CD81, and CD82, which are associated with the fusion involved in regeneration. Various integrin proteins, such as ITGA3 and ITGB1 positively regulate protein localization to plasma membrane. (Fig. 3d). $CD9^+$ EVs were closely related to regeneration of cells, induced by binding cell adhesion molecules, integrin, protein-containing complex (Fig. 3e and f and Table S7). On the contrary, $CD9^-$ EVs mainly exerted immune cell chemotaxis properties containing azurophil granule lumen, focal adhesin, and secretory granule (Figs. S4a and b).

We then confirmed whether $CD9^+$ EVs can enter cells more efficiently than $CD9^-$ EVs or total EVs. In the EV uptake assay, $CD9^+$ EVs showed greater adherence or entry into salivary epithelial cells compared to total EVs and $CD9^-$ EVs (Fig. 3g). Through the STRING database, we discovered that CD9, unlike tetraspanin proteins such as CD63 or CD81, interacts with the adhesion molecule CD44, which is well known and widely expressed in SGs. (Fig. 3h and Figs. S4c and d). Moreover, we confirmed the presence of CD44 in mouse submandibular glands and human parotid gland organoids by using IF staining (Fig. S4e) This analytical approach enabled us to uncover the complex proteomic profiles associated with these different EV subtypes, which illuminated their distinct cargo compositions and potential functional roles.

3.4. sgBPC-derived $CD9^+$ EVs restore SG hypofunction and attenuate SG fibrosis

To study the therapeutic effects of $CD9^+$ EVs on damaged SGs, we created an obstructive sialadenitis model by ligating the submandibular duct of mice. We surgically tied the SG duct, including the nerves and vessels, using suture materials and maintained it for 14 days to induce severe fibrotic changes in the SGs (Fig. 4a). We then infused EVs into the SG ducts for 3 consecutive days after de-ligation on post-ligation day 14. The SG size appeared

smaller in the phosphate-buffered saline (PBS)-treated group than in the EV-treated groups (Fig. 4b). We observed and measured the changes in body and SG weights, salivary flow rates (SFR), and lag time to salivation until 7 days after de-ligation (Fig. 4c–f). The mean SG weight decreased significantly after ligation. The retroductal delivery with $CD9^+$ EVs tended to increase the gland weight, although it did not significantly differ between groups (Fig. 4c). Ligation injury significantly delayed salivation, increasing lag time, and reduced the SFR even 7 days after de-ligation (Fig. 4d–f). These findings highlight the persistent functional impairments caused by the injury. However, both $CD9^-$ EV and $CD9^+$ EV-treated groups exhibited improvements in lag time (Fig. 4d), suggesting partial recovery of salivary gland function. Notably, the $CD9^+$ EV-treated group demonstrated a significantly improved SFR compared to the PBS-treated group (Fig. 4e). When normalized to body weight, the SFR of the $CD9^+$ EV-treated group (Fig. 4f) also showed substantial recovery, further supporting the therapeutic potential of $CD9^+$ EVs in promoting salivary gland function post-ligation.

Microscopic evaluation revealed distinct changes in the SGs treated with $CD9^-$ EVs and $CD9^+$ EVs compared to those treated with PBS. Although pilocarpine, which typically stimulates salivary secretion, was administered, it did not significantly affect the morphology of the SGs. This suggests that the observed histological changes were primarily due to the EV treatments rather than pilocarpine administration.

H&E staining quantification showed that the $CD9^+$ EV-treated group had significantly lower SG damage scores compared to both the PBS and $CD9^-$ EV-treated groups. The PBS group exhibited approximately 9 times more damage compared to the sham group, and the $CD9^-$ EV-treated group displayed 1.17 times more damage compared to the $CD9^+$ EV-treated group (Fig. 4g, h and Fig. S6).

PAS staining further demonstrated substantial regeneration of the acinar and ductal structures, including mucosubstance production, which was more prominent in the $CD9^+$ EV-treated group than in the PBS group (Fig. 4i and j). This analysis revealed that the mucosubstance area in the PBS group was reduced by approximately 2.82-fold compared to the sham group. Furthermore, the $CD9^+$ EV-treated group showed a 1.37-fold increase in mucosubstance area compared to the PBS group, and a 1.27-fold increase compared to the $CD9^-$ EV-treated group (Fig. 4i and j).

MTC staining revealed that the $CD9^+$ EV-treated group exhibited less periductal and perivascular fibrosis compared to the PBS group, as confirmed by densitometry (Fig. 4k and l). The fibrosis area in the PBS group was 32.5 times larger than that of the sham group. Meanwhile, the $CD9^+$ EV-treated group showed a 1.29-fold reduction in fibrosis compared to the $CD9^-$ EV group, and the PBS group had a 1.44-fold increase compared to the $CD9^-$ EV group (Fig. 4k and l).

Sirius red staining further indicated minimal collagen deposition in the sham group. In contrast, significant collagen accumulation was observed extending from the portal to the acinar and ductal septum areas 2 weeks post-ligation (Fig. 4m and n). Quantitative analysis revealed that the collagen area in the PBS group was approximately 20.67 times larger than that of the sham group. Moreover, the $CD9^+$ EV-treated group showed a 1.5-fold reduction in collagen area compared to the $CD9^-$ EV group, while the PBS group had a 1.48-fold increase in collagen compared to the $CD9^-$ EV group (Fig. 4m n).

Purified EVs were also injected after storage at −80 °C for 1, 3, and 6 months, and SG weight, lag time, and saliva volume showed improved results (Figs. S5a–c). H&E staining showed improved acinar-ductal structure in all $CD9^+$ EV-injected groups, while the PBS groups did not (Figs. S5d and e). The mucin production area measured by PAS staining showed a slight increase (Figs. S5f and g). The assessment of fibrosis area through MTC and Sirius red staining revealed a sustainable healing effect in EVs stored for 1, 3, and 6 months compared to the PBS-treated group (Figs. S5h–k). Overall, sgBPCs-derived $CD9^+$ EVs recovered SG dysfunction and fibrosis caused by duct ligation in mice and maintained their efficacy even after long-term cryopreservation.

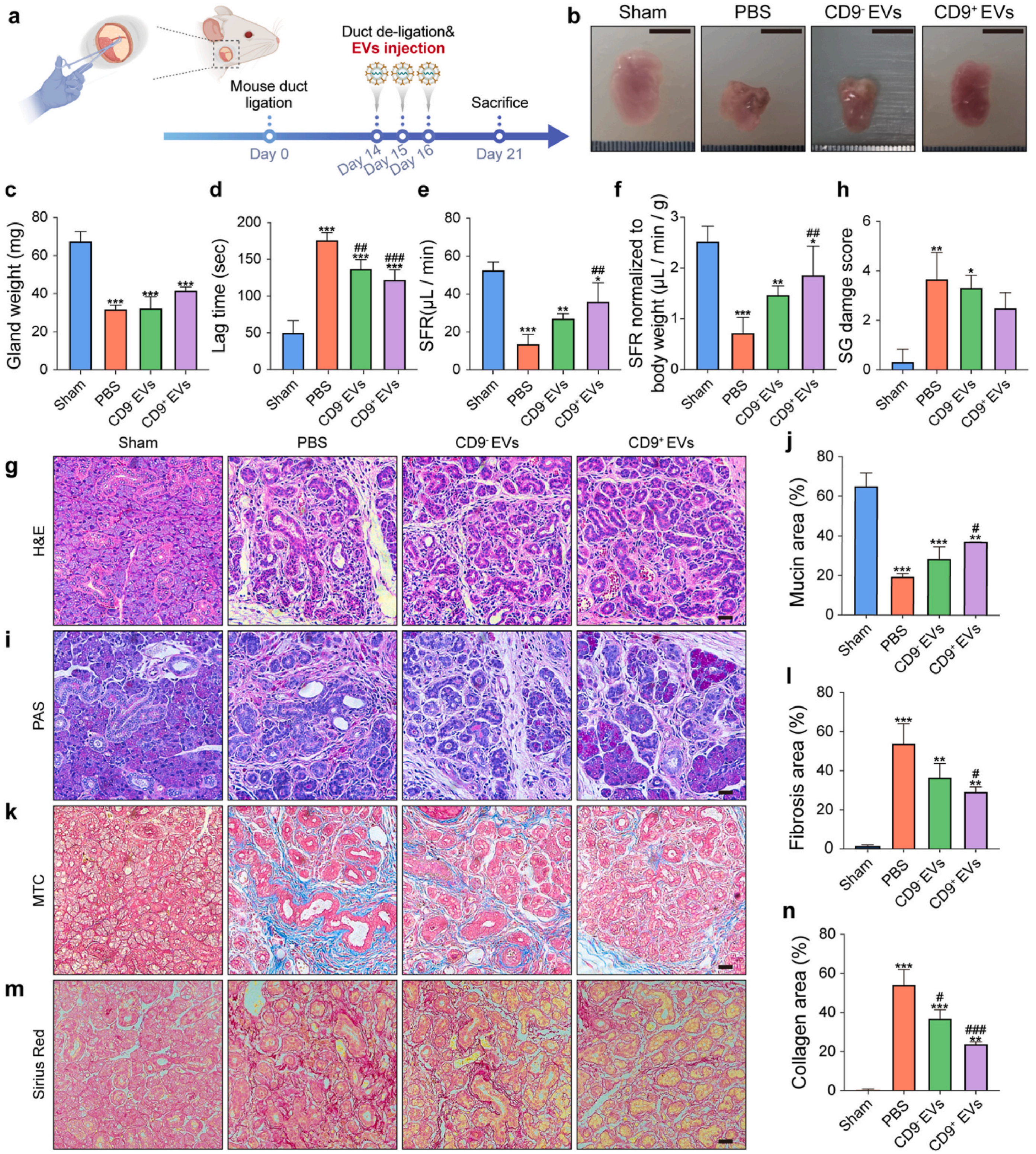

Fig. 4. Therapeutic effect of sgBPCs-derived EVs on SG fibrosis and hypofunction in a SG duct ligation model. (a) Schematic representation of the animal experiment for disease modeling and retroductal delivery. (b) Representative images of the SG at 1 week after ligation removal and EV treatment. (Scale bar = 10 mm). (c) SG weights measured at 1 week after de-ligation. (d) Lag time to salivation (sec) after pilocarpine stimulation at 1 week after de-ligation. (e) Saliva flow rate (SFR: μL/min) after stimulation at 1 week after de-ligation. (f) Saliva flow rate normalized to body weight (μL/min/g) after stimulation at 1 week after de-ligation. (g, i, k, m) H&E, PAS, MTC, and Sirius red staining performed at 1 week after ligation removal. (Scale bar indicates 25 μm). (g, h) Densitometric analyses performed by measuring the pixels of the acinar and ductal areas after H&E staining. The SG injury score was quantified based on the morphological disruption of acinar and ductal structures and cell loss after H&E imaging. (i, j) Magenta-colored mucin production areas after PAS staining. (k, l) Blue fibrotic lesion areas after MTC staining. (m, n) Red-colored collagen deposition areas after Sirius red staining. Untreated: Sham; PBS: De-ligation and PBS-injected control; CD9^{-} EVs: De-ligation + CD9^{-} EVs treatment; and CD9^{+} EVs: De-ligation + CD9^{+} EVs treatment. *Compared with untreated (Sham); $^{\#}$compared with PBS. as $*p$-value <0.05, $**p$ -value <0.01, and $***p$ -value <0.001 relative to the sham group, and $\#p$ -value <0.05, $\#\#p$ -value <0.01, and $\#\#\#p$ -value <0.001.

3.5. sgBPC-derived CD9$^+$ EVs inhibit epithelial-mesenchymal transition and fibrotic change

To further investigate *in vivo* mechanisms, we conducted immunofluorescence staining on various SG epithelial cells and their secreted proteins after administering EVs and waiting for 7 days. We did not observe any significant differences in the expression of basal cell marker KRT5, luminal cell marker KRT7 and myoepithelial cell marker ACTA2 among all groups (Figs. S7a and b). However, we found that submandibular gland protein c (SMGc)$^+$ cells, which indicate pro-acinar cells, were depleted after ligation and subsequently restored after EV injection with CD9$^+$ EVs, showing a significant recovery (Fig. S7a). Additionally, the number of MIST1$^+$ cells, representing both progenitor cells and mature acinar cells, significantly decreased after ligation (Fig. S7b). PSP (parotid secretory protein, BPIFA2), known to play a surfactant role in SGs and be present in serum during injury, was observed in the ligation group and CD9$^-$ EVs-treated group. However, it was not observed in the sham group and CD9$^+$ EVs-treated group (Fig. S7b). We observed that an increase in CDH2, which is a marker for fibrosis and epithelial-mesenchymal transition (EMT) processes, occurred in the ligation group. However, both CD9$^-$ EVs and CD9$^+$ EVs-treated group led to a decrease in CDH2 (Fig. S7c). Additionally, epithelial cell marker CDH1 decreased in the PBS-treated group but was restored in both EV-treated groups (Fig. S7c). Vimentin (VIM), which is also considered a marker for fibrosis and EMT, did not increase with ligation and showed no changes with EV treatment (Fig. S7c). Furthermore, the differences in cell death and proliferation in SG cells induced by ligation and EV administration were examined. Cleaved caspase-3, a marker for cell apoptosis, did not exhibit prominent staining in any group (Fig. S7d). However, cell proliferation, assessed through MKI67, significantly decreased with ligation, and was restored by EVs. CD9$^+$ EVs showed substantial recovery in cell proliferation (Fig. S7d). All these findings were validated through quantification of immunofluorescence staining (Figs. S8a–k). Taken together, our findings indicate that CD9$^+$ EVs demonstrated therapeutic efficacy in the duct ligation fibrosis model by suppressing EMT and promoting proliferation of SG cells.

3.6. sgBPC-derived CD9$^+$ EVs enhance the cell uptake and regeneration in ex vivo organoid fibrosis model

Based on the demonstrated SG healing and anti-fibrotic effects of CD9$^+$ EVs in the *in vivo* duct ligation model, we aimed to investigate the underlying mechanisms of CD9$^+$ EVs using an *in vitro* human SG organoid system. Since organoids are cultured within ECM, such as Matrigel™, we first verified whether the organoid cells could uptake the EVs. Initially, we treated the culture medium with 10^7 particles/mL of DiI-stained EVs and observed the outermost layers of the organoids after 24 h of incubation (Fig. S9a). Activin A, known for inducing epithelial-mesenchymal transition (EMT), acinar to ductal metaplasia (ADM), and fibrosis in various organs such as the liver, pancreas, and lung, was applied to the organoids. These processes—EMT, ADM, and fibrosis—are similar to the pathological changes observed in ligated salivary glands. To establish a pro-fibrotic environment, we reduced the concentration of the TGFβ inhibitor A83-01 from 5 μM to 1 μM in the culture medium, and on the sixth day, we supplemented the medium with 20 ng/mL of Activin A (Fig. S9b).

The pro-fibrotic organoids were treated for an additional 48 h with media containing either CD9$^+$ EVs, CD9$^-$ EVs, or dexamethasone (DEXA). DEXA is widely used as a positive control in the treatment of inflammatory salivary gland diseases. In our previous studies, dexamethasone has shown strong anti-inflammatory properties by reducing glandular inflammation and partially restoring function in mouse models of sialadenitis induced by duct ligation [50]. In vitro experiments with salivary gland organoids also demonstrated that macrophage polarization was shifted toward an anti-inflammatory phenotype when exposed to DEXA-conditioned medium. Consequently, in this experiment, we used DEXA as a benchmark to compare its known anti-inflammatory effects with those of our experimental EV treatments under fibrotic organoid culture conditions. Although Activin A did not alter the size of the organoids, it inhibited their growth, and DEXA could not overcome this growth inhibition. However, CD9$^-$ EVs partially restored the growth inhibition caused by Activin A, and CD9$^+$ EVs exhibited a higher level of cell growth recovery compared to CD9$^-$ EVs (Fig. 5a and Figs. S9c and d). Moreover, a tendency for decreased expression of *ACVR1* was observed in all groups treated with dexamethasone and EVs, but CD9$^+$ EVs showed levels most similar to those of the untreated groups (Fig. S9e). Additionally, we confirmed by Western blot that both CD9$^-$ EVs and CD9$^+$ EVs reduced the phosphorylation of SMAD2/3 in organoids treated with Activin A, whereas dexamethasone treatment did not achieve this reduction (Fig. S9f). Furthermore, H&E staining revealed that metaplasia, which is not typically found in normal parotid gland-derived organoids, was observed when Activin A was supplied (Fig. 5b). DEXA did not significantly alleviate this effect. However, both CD9$^-$ EVs and CD9$^+$ EVs mitigated the metaplasia, with CD9$^+$ EVs showing a more pronounced effect (Fig. 5b). Furthermore, PAS staining demonstrated that organoids treated with Activin A exhibited a significant increase in mucin production in the luminal space, despite parotid gland-derived organoids normally containing little mucin (Fig. 5c). While the dexamethasone-treated group did not reduce mucin levels, treatment with EVs, especially CD9$^+$ EVs, resulted in decreased mucin production (Fig. 5c).Moreover, Sirius red staining of the organoids revealed red-stained areas indicative of fibrosis in the groups treated with Activin A or Activin A with DEXA, whereas these stained areas were reduced in the groups treated with either CD9$^-$ EVs or CD9$^+$ EVs (Fig. 5d). Furthermore, excessive Activin A is known to inhibit normal cell differentiation in SGs. In organoids treated with Activin A, the expression of differentiation markers KRT7, AQP5 and AMY1 were scarcely detected (Fig. 5e and f). While the addition of DEXA did not significantly improve these pathological manifestations, EV treatment resulted in notable improvements, with CD9$^+$ EVs showing the most pronounced effect (Fig. 5e and f). Additionally, the measurement of gene expression levels for *KRT7*, *AQP5*, and *AMY1* for quantitative analysis showed a similar trend to the immunofluorescence staining results (Fig. 5h–j).

Next, we investigated whether epithelial-mesenchymal transition (EMT), which precedes fibrosis, is induced by Activin A and whether it is alleviated by treatment with dexamethasone or EVs. Human SG organoids treated with Activin A exhibited expression of CDH2 (N-cadherin; mesenchymal cell marker) at the outermost layer, while the expression of CDH1 (E-cadherin; epithelial cell marker) was reduced in these peripheral cells (Fig. 5g). The addition of dexamethasone did not significantly alter CDH2 expression in the outer layer. However, treatment with CD9$^-$ EVs or CD9$^+$ EVs reduced CDH2 expression and restored CDH1 expression. Immunofluorescence staining was followed by an investigation into the expression of various EMT and fibrosis-related genes using SG organoids. Activin A treatment increased the expression of EMT and fibrosis-associated genes, including *TGFB1, TGFB2, SMAD2, SMAD3, SNAIL, SLUG, TWIST1, ZEB1,* and *ZEB2* (Figs. S10a and b). *TGFB1* and *TGFB2* initiated the TGFβ signaling pathway, which, through *SMAD2* and *SMAD3*, promoted EMT and fibrosis. Transcription factors such as *SNAIL, SLUG, TWIST1, ZEB1,* and *ZEB2* were upregulated, leading to mesenchymal cell characteristics, and further promoting EMT (Figs. S10a and b). The expression of the epithelial marker *CDH1* (E-cadherin) decreased, while mesenchymal markers *CDH2* (N-cadherin) and *VIM* (Vimentin) increased, indicating a loss of cell-cell adhesion and enhanced cell motility, signifying EMT progression (Fig. S10b). Additionally, fibrosis-related genes such as *FN1* (Fibronectin 1), *ACTA2* (Alpha-Smooth Muscle Actin), *COL1A1*, and *COL3A1* were upregulated, contributing to extracellular matrix (ECM) composition and increased tissue stiffness, leading to fibrosis (Fig. S10c). Conversely, the expression of *MMP2*, an enzyme responsible for degrading ECM components, decreased, while *TIMP1* and *TIMP2*, inhibitors of MMPs,

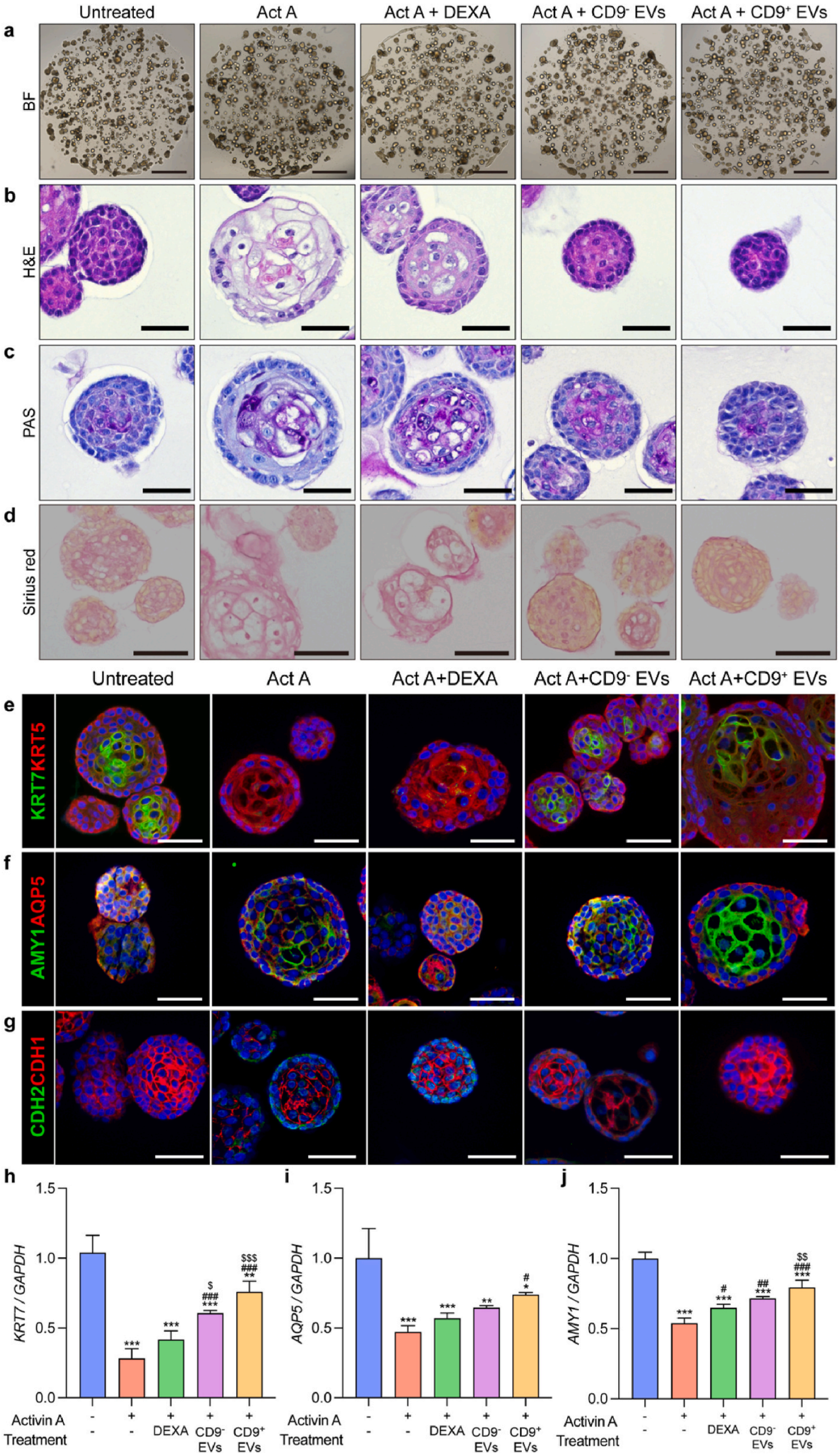

Fig. 5. Biological properties of sgBPCs-derived EVs in 3D organoid cultures. (a) Human parotid gland organoid bright images treated with Activin A, dexamethasone, $CD9^-$ EVs, and $CD9^+$ EVs. Scale bar indicates 500 μm. (b–d) Representative images of Activin A-treated organoids stained with H&E, PAS, and Sirius red staining. Scale bar indicates 50 μm. (e–g) Representative immunofluorescences images of Activin A-treated organoids stained with KRT7 (green), KRT5 (red), AMY1 (green), AQP5 (red), CDH2 (green), and CDH1 (red). Scale bar indicates 50 μm. (h–j) Relative expression of SGs epithelial cell related genes (*KRT7, AQP5, AMY1*) (n = 3, *, $^{\#}$, $^{\$}$ considered as statistically significant). *Compared with untreated; $^{\#}$compared with Activin A; and $^{\$}$compared with Activin A + DEXA.

were upregulated, promoting excessive ECM accumulation (Fig. S10c). In the dexamethasone-treated group, a slight recovery toward normal gene expression levels was observed, though the overall effect remained minimal. In contrast, the group treated with CD9⁺ EVs exhibited significant improvement. CD9⁺ EVs effectively reduced the elevated expression of *TGFB1, TGFB2, SMAD2, SMAD3, SNAIL, SLUG, TWIST1, ZEB1, ZEB2, CDH2, VIM, FN1, ACTA2, COL1A1, COL3A1, TIMP1,* and *TIMP2* induced by Activin A. Additionally, they increased the expression of *CDH1* and *MMP2*, suppressing EMT and fibrosis processes. While the CD9⁻ EVs group showed some improvement, the effects were less pronounced compared to the CD9⁺ EVs group. These findings suggest that CD9⁺ EVs effectively inhibit Activin A-induced EMT and fibrosis,

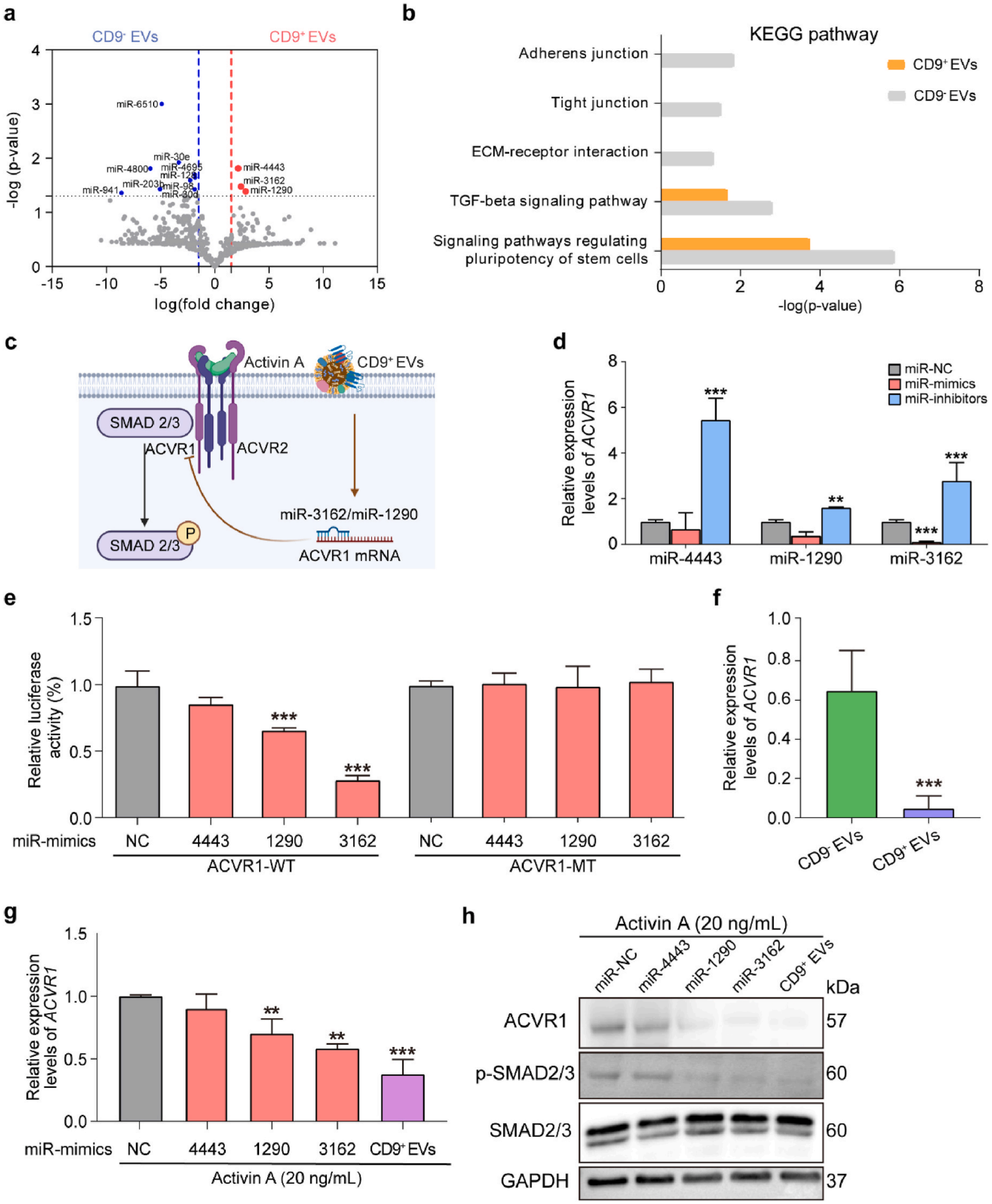

Fig. 6. Anti-fibrotic role of EV-miRNA in sgBPCs-derived EVs. (a) Volcano plot showing the significantly enriched miRNAs in CD9⁻ EVs and CD9⁺ EVs. (b) KEGG pathway for target mRNAs of miRNAs in CD9⁺ EVs and CD9⁻ EVs. (c) Predicted target ACVR1 in ACVR1/SMAD signaling pathway. (d) Relative expression levels of *ACVR1* after incubation with inhibitor and mimics of each miRNA (miR-4443, miR-3162, and miR-1290) for 24 h. (e) Luciferase activity assay was used to detect the interaction between miR-4443, miR-1290, miR-3162, and *ACVR1*. (f) Relative expression levels of *ACVR1* after incubation of CD9⁻ EVs and CD9⁺ EVs. (g) Relative expression levels of *ACVR1* after inducing 20 ng/mL of activin, followed by the treatment of miR-NC, miR-4443, miR-1290, miR-3162, and CD9⁺ EVs for 24 h. (h) Western blot of ACVR1, phosphorylation of SMAD2/3, SMAD2/3 and GAPDH after inducing the 20 ng/mL of activin, followed by treatment with the miRNAs or CD9⁺ EVs (***p*-value <0.01 and ****p*-value <0.001).

highlighting their potential as a therapeutic strategy for SG diseases. These findings suggest that sgBPC-derived EVs could be effective in reducing SG fibrosis induced by Activin A or other disorders where Activin A plays a crucial role.

3.7. EV miRNAs in sgBPC-derived CD9$^+$ EVs promote an anti-fibrotic effect

To elucidate the therapeutic mechanisms of CD9$^+$ EVs in our fibrosis models, we investigated the role of miRNAs, which play a crucial role in regulating gene expression. The EV miRNA-seq revealed distinct patterns of differential expression between CD9$^+$ EVs and CD9$^-$ EVs (Fig. 6a). By analyzing RNA-seq data, we focused on 12 miRNAs that showed significant change in either up-regulation or down-regulation in CD9$^+$ EVs. Applying rigorous criteria of $|\log2 \text{ fold change}|>1$ and an adjusted p-value <0.05, a subset of genes was identified for further investigation (Fig. 6a). Three miRNAs namely, miR-4443, miR-1290, and miR-3162, which were upregulated in CD9$^+$ EVs, were found to be significant. By employing Kyoto Encyclopedia of Genes and Genomes (KEGG) pathway enrichment, we identified potential pathways influenced by these miRNAs (Tables S8 and S9). Notably, the miRNAs of CD9$^+$ EVs and CD9$^-$ EVs were both associated with signaling pathways regulating pluripotency of stem cells and TGFβ signaling pathway (Fig. 6b). However, the miRNAs-enriched by CD9$^-$ EVs induced the downregulation of adherence, tight junction, and ECM-receptor interaction, which leads to inhibit the interaction of the cells and EVs (Fig. 6b).

The convergence of predictions from tools like miR-DB, DIANA, and TargetScan pinpointed *ACVR1*, a fibrosis inducer linked with Activin signaling, as a prominent target (Fig. 6c and Figs. S11a–c). We confirmed the relationship between *ACVR1* and miRNA through RT-qPCR after transfecting specific miR mimics and inhibitors (Fig. 6d and Figs. S11d–f and Table S2). It was observed that miR-3162 and miR-1290 mimics reduced *ACVR1* mRNA levels, whereas all three inhibitors increased them. Further experiments, including a dual-luciferase reporter assay, confirmed that miR-3162 and miR-1290 directly targeted *ACVR1* (Fig. 6e and Fig. S11g). When we examined the effect of CD9$^+$ EVs on *ACVR1*, we found that CD9$^+$ EVs significantly suppressed ACVR1 compared to CD9$^-$ EVs (Fig. 6f). Subsequently, a detailed analysis following the introduction of Activin A showed that miR-3162, miR-1290, and CD9$^+$ EVs all suppressed ACVR1 and SMAD2/3 phosphorylation (Fig. 6g and h). Collectively, these results suggest that miR-3162 and miR-1290 in CD9$^+$ EVs reduce ACVR1 expression and inhibit fibrosis by suppressing the phosphorylation of SMAD2/3 via the Activin-ACVR1 axis (Fig. S10h).

Collectively, these results suggest that miR-3162 and miR-1290 in CD9$^+$ EVs reduce ACVR1 expression and inhibit fibrosis by suppressing the phosphorylation of SMAD2/3 via the Activin-ACVR1 axis (Fig. S11h).

4. Discussion

In this study, we have demonstrated that CD9$^+$ EVs derived from sgBPCs effectively attenuate fibrosis and promote regeneration in SG diseases. Specifically, CD9$^+$ EVs exhibited superior anti-fibrotic effects compared to CD9$^-$ EVs, as evidenced by reduced collagen deposition and restored acinar structures *in vivo*, and enhanced organoid formation *ex vivo*. Notably, miR-3162 and miR-1290 enriched in CD9$^+$ EVs directly targeted fibrotic genes such as ACVR1, leading to the suppression of fibrosis-related pathways in SG tissues. These findings highlight the potential of sgBPC-derived EVs as a targeted therapeutic approach for SG fibrosis, providing a foundation for precision medicine in treating SG disorders. In this study, the potential of CD9$^+$ EVs derived from sgBPCs had been successfully observed as a promising therapeutic approach for counteracting fibrosis and promoting regeneration.

While utilizing EVs harvested from stem or progenitor cells derived from specific tissues holds great potential for treating diseases associated with that organ [64], obtaining and culturing sufficient quantities of tissue-specific epithelial or mesenchymal stem cells for EV isolation is considerably more challenging than sourcing them from readily available tissues like discarded fat or Wharton's jelly [65–67]. In the context of SG diseases, EVs obtained from SG-specific cells are likely to offer more organ-specific therapeutic effects compared to those derived from commonly used sources like bone marrow or adipose tissue-derived mesenchymal stem cells (MSCs) as evidenced by our previous study demonstrating the superior efficacy of MSCs obtained from SGs in addressing SG inflammation [49] To overcome the challenges of EV production from tissue-specific cells, recent methods have been proposed to enhance EV production by subjecting cells to mild stress or using small molecules [68–71]. In line with these findings, our study leveraged microfluidic technology and utilized inhibition of Activin receptor-like kinase (ALK) 1–7 through A83-01 and LDN193189 to increase EV secretion from sgBPCs, not only maintaining cell viability but also boosting EV production specific to SG tissue [72–74]. By addressing SG fibrosis via retrograde ductal delivery of these enhanced EVs, our study offers a promising avenue for targeted treatment, representing significant steps towards precision medicine for SG disorders.

Despite homogeneous cell cultures, secreted exosomes can exhibit heterogeneity in surface markers and its cargo [68]. Various studies have been published to categorize cell-specific or functional exosomes [35,75]. We decided to use CD9 as the marker for isolating EVs from cultured sgBPCs in this experiment, as it is highly expressed in undifferentiated sgBPCs and also present in basal cells of SGs. In addition, CD9 is capable of binding to both ITGB1 and CD44, which are present in almost all regions of the SG cell membrane. EVs derived from pancreatic cancer in the exocrine pancreas are known to be unable to be taken up by other exocrine pancreatic cells mainly composed of acinar cells when CD9 is artificially depleted or blocked [76,77]. These suggest CD9 an efficient choice for delivery. The CD9$^+$ EVs contain a high amount of membrane surface proteins, integrins, and exosomes that aid in intracellular uptake and movement, promoting tissue regeneration [78,79]. The identified surface protein markers of CD9$^+$ EVs are closely related to the protein-protein interaction (PPI) network, which is an essential component of plasma and cell junctions. These proteins induce transporter activity and integrin binding, leading to cell regeneration or migration. Studies have shown that ITGB1 and ITGA3 are involved in epithelial morphogenesis and skin wound regeneration [78,79]. On the other hand, CD9$^-$ EVs contain secretory granules, lysosomes, and endoplasmic reticulum-related proteins that activate proteinases and peptidases (Fig. S4b). Biological properties of CD9$^-$ EVs focus on regulating immunogenicity, such as T-cell and lymphocyte chemotaxis (Fig. S4a) which is differential features of CD9$^+$ EVs. EV miRNAs are small RNA molecules that are crucial in regulating various biological processes [80]. They play an important role in controlling the expression of target genes [81].

Two specific miRNAs, miR-3162 and miR-1290, have been identified as key regulators that directly target ACVR1 and reduce SMAD2/3 phosphorylation. Our research has shown that CD9$^+$ EVs significantly downregulate the expression levels of ACVR1 compared to CD9 EVs. This suggests that activated ACVR1 is regulated by CD9$^+$ EVs, which contain higher levels of miR-1290 and miR-3162, and that the anti-fibrotic effect of CD9$^+$ EVs is due to these specific miRNAs. Moreover, the miRNAs encapsulated in CD9$^+$ EVs were predicted by bioinformatics tools to inhibit the TGFβ pathway, a key fibrosis mechanism [82]. Although CD9$^-$ EVs exhibit a slightly inferior ability to dock onto cells compared to CD9$^+$ EVs, it is speculated that they exert anti-fibrotic effects in *in vitro* organoid cultures or *in vivo* ductal obstruction models. Further research would determine which miRNAs encapsulated within exosomes are effective in anti-fibrosis, it would be possible to use more efficient anti-fibrotic substances and delivery strategies through artificial EVs or EV replacement.

miR-3162 has been shown to exert anti-inflammatory and anti-fibrotic effects. It modulates cellular processes in cardiac fibrosis, suggesting its potential role in tissue fibrosis regulation [83,84]. miR-1290 is downregulated in patients with oral submucous fibrosis, myocardial infarction, and lung inflammation suggesting its potential role in inhibiting fibrotic processes [85–87]. These findings support the idea that miR-1290 may possess anti-fibrotic properties and could be a therapeutic target for fibrotic diseases. In this study, we have shown that CD9$^+$ EVs have a functional advantage in regenerating SG cells and restoring SG function during the recovery period after SG duct obstruction, which can cause severe fibrotic changes. Basal cells in many glandular tissues are maintained through dual SMAD inhibition by the intrinsic microenvironment. CD9$^+$ EVs contain high levels of miRNAs that help inhibit Activin A signals. When these EVs were administered by retroductal delivery after SG duct blockage was relieved in mice, they were delivered to salivary epithelial cells, leading to repopulation of SMGc$^+$ pro-acinars, MIST1$^+$ mature acinar, and KI67$^+$ proliferating cells. We also observed that these EVs had excellent stability for 6 months, both in terms of their structure, cargo molecules, and healing potential (Fig. 2k-n and Fig. S5). Previous studies have suggested that EVs are resistant to enzymatic degradation and can withstand freeze-thaw cycles, making them easier to store and transport compared to live cells [88]. These properties of CD9$^+$ EVs make them ideal for clinical applications.

Organoid models, distinct from 2D cell cultures, closely mimic organs, making them highly effective for studying the impact of drugs on tissues. Especially in the case of SGs, which are bi-layered organs with cell polarity, and where primary acinar cells cannot be maintained in 2D cell cultures, organoid models are essential for mechanistic studies. Based on our previously published method for establishing SG organoids [51], we induced various EMT and fibrosis in SG epithelial cells by excessive treatment with Activin A and demonstrated their normalization by EVs, as confirmed through special staining, fluorescence staining, and RT-qPCR. Although our organoid models demonstrated the impact of CD9$^+$ EVs on epithelial-to-mesenchymal transition (EMT) and fibrosis, these processes also involve fibroblast-to-myofibroblast transformation, which is not fully captured in the current models. Future research should focus on developing more precise models, such as assembloids, that incorporate both epithelial cells and fibroblasts to better reflect the complex tissue interactions involved in EMT and fibrosis. It is also essential to validate the therapeutic effects and safety of CD9$^+$ EVs in animal models. Additionally, due to the heterogeneity in size and content of CD9$^+$ EVs, advancing techniques to selectively enrich specific vesicle subpopulations with desired therapeutic properties will enhance treatment precision and efficacy.

Given that fibrosis in the parotid gland involves similar pathological processes as fibrosis in other tissues such as inflammation, extracellular matrix deposition, and fibroblast activation, we believe that CD9$^+$ EVs could play a therapeutic role in mitigating these processes. Furthermore, research has shown that EVs possess a range of bioactive molecules (proteins, lipids, and RNAs) that can modulate inflammation, promote tissue repair, and reduce fibrosis. These effects have been observed not only in the tissues from which the EVs were derived but also in distant organs. For instance, EVs produced from bone marrow-derived or adipose-derived stem cells have been utilized to promote recovery and exert anti-inflammatory effects in organs such as the heart, liver, and kidneys, which are unrelated to the bone marrow or adipose tissue. This broader applicability suggests that CD9$^+$ EVs from SG epithelial cells could potentially be used for fibrosis and disease treatment in other organs beyond the SGs.

In the mouse model of duct ligation, where the duct, blood vessels, and nerves are ligated to induce more severe damage and leads to partial necrosis, making complete tissue recovery unachievable. Most recovery in duct ligation models occurs within 1–2 weeks after de-ligation, so even with long-term observation, significant differences in recovery are not expected. Additionally, due to the natural progression of fibrosis with aging, observing the effects at much later time points may make it harder to discern differences. Furthermore, because recovery happens quickly, we believe that administering EVs continuously immediately after de-ligation is beneficial to suppress duct obstruction early on.

Our findings suggest distinct antifibrotic effects between CD9$^+$ and CD9$^-$ EVs, with CD9$^-$ EVs potentially influencing fibrosis indirectly through immune modulation, as indicated by in silico analyses. Future research should validate these effects experimentally, explore their efficacy in other disease models such as autoimmune sialadenitis or radiation-induced damage, and conduct long-term follow-up studies to assess the durability of these therapies. Such studies will help clarify the therapeutic potential and mechanisms of CD9$^+$ and CD9$^-$ EVs across different pathological contexts.

5. Conclusions

In summary, we have shown that EVs derived from sgBPCs have a positive impact on the proliferation, wound healing, and anti-fibrotic regeneration of SGs in both *in vitro* and *ex vivo* organoid models. Specifically, in the *in vivo* SMG model, CD9$^+$ EVs effectively reduced fibrosis and enhanced tissue regeneration, confirming their superior therapeutic potential compared to CD9$^-$ EVs and controls. This advancement in EV-based therapy offers promising avenues for precise regenerative medicine, including organ-specific cell and EV isolation, targeted delivery, functional EV purification, and long-term stability with efficacy. However, further research on regulatory approval and standardization of production methods is crucial for their clinical expansion.

CRediT authorship contribution statement

Sunyoung Park: Writing – original draft, Visualization, Methodology, Formal analysis, Data curation. **Yeo-Jun Yoon:** Writing – original draft, Visualization, Methodology, Formal analysis. **Yongpyo Hong:** Validation, Methodology, Investigation. **Jianning Yu:** Validation, Methodology, Investigation. **Jae-Min Cho:** Visualization, Methodology. **Ye Jin Jeong:** Methodology. **Haeun Yu:** Methodology. **Hyorim Jeong:** Methodology. **Hyunjin Lee:** Methodology. **Seungyeon Hwang:** Methodology. **Won-Gun Koh:** Conceptualization. **Ji Yeong Yang:** Methodology. **Kyung-A Hyun:** Conceptualization. **Hyo-Il Jung:** Writing – review & editing, Supervision, Project administration, Funding acquisition. **Jae-Yol Lim:** Writing – review & editing, Supervision, Project administration, Funding acquisition.

Ethics approval and consent to participate

All procedures were approved by the Institutional Animal Care and Use Committee of the Yonsei University College of Medicine and conformed to the Avison Biomedical Research Center guidelines (approval number: 2022–0051). Human sgBPCs were prepared from normal tissue samples of patients who underwent parotidectomy for a benign parotid tumor, after obtaining informed consent and approval from the institutional review board (permission number #2017-0226-001).

Declaration of competing interest

The authors declare the following personal relationships which may be considered as potential competing interests: Sunyoung Park, Hyorim Jeong, Hyunjin Lee, Ji Yeong Yang and Hyo-Il Jung are currently employed by The DABOM Inc.

Acknowledgments

This study was conducted in part at the Yonsei Advanced imaging Center in cooperation with Carl Zeiss Microscopy and Flow Cytometry Center. This work was supported by the National Research Foundation (NRF) of Korea funded by the Ministry of Science and ICT (2020M3A9I4039045, 2021R1A2C3011254, and RS-2024-00432946);

and the Basic Science Research Program through the NRF funded by the Ministry of Education(2022R1I1A1A01072997). Faculty Research Grant funded by the Gangnam Severance Hospital- College of Engineering in Yonsei University (D-2023-0011).

Appendix A. Supplementary data

Supplementary data to this article can be found online at https://doi.org/10.1016/j.bioactmat.2025.01.019.

References

[1] G.C. Blitzer, T. Glazer, A. Burr, S. Gustafson, O. Ganz, R. Meyers, K.A. McDowell, K. P. Nickel, R.J. Mattison, M. Weiss, R. Chappell, N.M. Rogus-Pulia, J. Galipeau, R. J. Kimple, Marrow-Derived Autologous Stromal Cells for the Restoration of Salivary Hypofunction (MARSH): a pilot, first-in-human study of interferon gamma-stimulated marrow mesenchymal stromal cells for treatment of radiation-induced xerostomia, Cytotherapy 25 (11) (2023) 1139–1144.

[2] G.C. Blitzer, N.M. Rogus-Pulia, R.J. Mattison, T. Varghese, O. Ganz, R. Chappell, J. Galipeau, K.A. McDowell, R.O. Meyers, T.A. Glazer, R.J. Kimple, Marrow-derived autologous stromal cells for the restoration of salivary hypofunction (MARSH): study protocol for a phase 1 dose-escalation trial of patients with xerostomia after radiation therapy for head and neck cancer: MARSH: marrow-derived autologous stromal cells for the restoration of salivary hypofunction, Cytotherapy 24 (5) (2022) 534–543.

[3] C. Gronhoj, D.H. Jensen, P. Vester-Glowinski, S.B. Jensen, A. Bardow, R.S. Oliveri, L.M. Fog, L. Specht, C. Thomsen, S. Darkner, M. Jensen, V. Muller, K. Kiss, T. Agander, E. Andersen, A. Fischer-Nielsen, C. von Buchwald, Safety and efficacy of mesenchymal stem cells for radiation-induced xerostomia: a randomized, placebo-controlled phase 1/2 trial (MESRIX), Int. J. Radiat. Oncol. Biol. Phys. 101 (3) (2018) 581–592.

[4] K.K. Jakobsen, A.F. Carlander, C. Gronhoj, T. Todsen, J. Melchiors, N. Paaske, A.K. O. Madsen, J. Kastrup, A. Ekblond, M. Haack-Sorensen, M. Farhadi, C. Maare, J. Friborg, C.D. Lynggard, C. von Buchwald, Effectiveness and safety of mesenchymal stem/stromal cell for radiation-induced hyposalivation and xerostomia in previous head and neck cancer patients (MESRIX-III): a study protocol for a single-centre, double-blinded, randomised, placebo-controlled, phase II study, Trials 24 (1) (2023) 567.

[5] K.K. Jakobsen, A.F. Carlander, T. Todsen, J. Melchiors, N. Paaske, A.K. Ostergaard Madsen, S. Kloch Bendtsen, C. Mordhorst, H. Stampe, J. Kastrup, A. Ekblond, M. Haack-Sorensen, M. Farhadi, C. Maare, J. Friborg, C.D. Lynggaard, A. Werner Hauge, R. Christensen, C. Gronhoj, C. von Buchwald, Mesenchymal stem/stromal cell therapy for radiation-induced xerostomia in previous head and neck cancer patients: a phase II randomized, placebo-controlled trial, Clin. Cancer Res. 30 (10) (2024) 2078–2084.

[6] K.K. Jakobsen, C.D. Lynggaard, N. Paaske, A.F. Carlander, J. Kastrup, A.W. Hauge, R. Christensen, C. Gronhoj, C.V. Buchwald, Long-term outcome following treatment with allogeneic mesenchymal stem/stromal cells for radiation-induced hyposalivation and xerostomia, Stem Cells Transl Med 13 (6) (2024) 515–521.

[7] C.D. Lynggaard, C. Gronhoj, R. Christensen, A. Fischer-Nielsen, J. Melchiors, L. Specht, E. Andersen, J. Mortensen, P. Oturai, G.H. Barfod, E.K. Haastrup, M. Moller-Hansen, M. Haack-Sorensen, A. Ekblond, J. Kastrup, S.B. Jensen, C. von Buchwald, Intraglandular off-the-shelf allogeneic mesenchymal stem cell treatment in patients with radiation-induced xerostomia: a safety study (MESRIX-II), Stem Cells Transl Med 11 (5) (2022) 478–489.

[8] C.D. Lynggaard, C. Gronhoj, S.B. Jensen, R. Christensen, L. Specht, E. Andersen, T. T. Andersen, U.M. Ciochon, G.S. Rathje, A.E. Hansen, H. Stampe, A. Fischer-Nielsen, C. von Buchwald, Long-term safety of treatment with autologous mesenchymal stem cells in patients with radiation-induced xerostomia: primary results of the MESRIX phase I/II randomized trial, Clin. Cancer Res. 28 (13) (2022) 2890–2897.

[9] X. Zhang, J.S. Yun, D. Han, J.I. Yook, H.S. Kim, E.S. Cho, TGF-Beta pathway in salivary gland fibrosis, Int. J. Mol. Sci. 21 (23) (2020).

[10] H.J. Hong, J.M. Cho, Y.J. Yoon, D. Choi, S. Lee, H. Lee, S. Ahn, W.G. Koh, J.Y. Lim, Thermoresponsive fiber-based microwells capable of formation and retrieval of salivary gland stem cell spheroids for the regeneration of irradiation-damaged salivary glands, J. Tissue Eng. 13 (2022) 20417314221085645.

[11] D.H. Jensen, R.S. Oliveri, S.F. Trojahn Kolle, A. Fischer-Nielsen, L. Specht, A. Bardow, C. Buchwald, Mesenchymal stem cell therapy for salivary gland dysfunction and xerostomia: a systematic review of preclinical studies, Oral Surg Oral Med Oral Pathol Oral Radiol 117 (3) (2014) 335–342, e1.

[12] J.W. Kim, J.M. Kim, M.E. Choi, S.K. Kim, Y.M. Kim, J.S. Choi, Adipose-derived mesenchymal stem cells regenerate radioiodine-induced salivary gland damage in a murine model, Sci. Rep. 9 (1) (2019) 15752.

[13] T. Kojima, S. Kanemaru, S. Hirano, I. Tateya, S. Ohno, T. Nakamura, J. Ito, Regeneration of radiation damaged salivary glands with adipose-derived stromal cells, Laryngoscope 121 (9) (2011) 1864–1869.

[14] J.Y. Lim, J.C. Ra, I.S. Shin, Y.H. Jang, H.Y. An, J.S. Choi, W.C. Kim, Y.M. Kim, Systemic transplantation of human adipose tissue-derived mesenchymal stem cells for the regeneration of irradiation-induced salivary gland damage, PLoS One 8 (8) (2013) e71167.

[15] J.Y. Lim, T. Yi, J.S. Choi, Y.H. Jang, S. Lee, H.J. Kim, S.U. Song, Y.M. Kim, Intraglandular transplantation of bone marrow-derived clonal mesenchymal stem cells for amelioration of post-irradiation salivary gland damage, Oral Oncol. 49 (2) (2013) 136–143.

[16] Y. Sumita, Y. Liu, S. Khalili, O.M. Maria, D. Xia, S. Key, A.P. Cotrim, E. Mezey, S. D. Tran, Bone marrow-derived cells rescue salivary gland function in mice with head and neck irradiation, Int. J. Biochem. Cell Biol. 43 (1) (2011) 80–87.

[17] X. Fu, The immunogenicity of cells derived from induced pluripotent stem cells, Cell. Mol. Immunol. 11 (1) (2014) 14–16.

[18] C.A. Herberts, M.S. Kwa, H.P. Hermsen, Risk factors in the development of stem cell therapy, J. Transl. Med. 9 (2011) 29.

[19] D.M. Hoang, P.T. Pham, T.Q. Bach, A.T.L. Ngo, Q.T. Nguyen, T.T.K. Phan, G. H. Nguyen, P.T.T. Le, V.T. Hoang, N.R. Forsyth, M. Heke, L.T. Nguyen, Stem cell-based therapy for human diseases, Signal Transduct. Targeted Ther. 7 (1) (2022) 272.

[20] A.S. Lee, C. Tang, M.S. Rao, I.L. Weissman, J.C. Wu, Tumorigenicity as a clinical hurdle for pluripotent stem cell therapies, Nat. Med. 19 (8) (2013) 998–1004.

[21] P. Lohan, O. Treacy, M.D. Griffin, T. Ritter, A.E. Ryan, Anti-donor immune responses elicited by allogeneic mesenchymal stem cells and their extracellular vesicles: are we still learning? Front. Immunol. 8 (2017) 1626.

[22] S. Du, Y. Guan, A. Xie, Z. Yan, S. Gao, W. Li, L. Rao, X. Chen, T. Chen, Extracellular vesicles: a rising star for therapeutics and drug delivery, J. Nanobiotechnol. 21 (1) (2023) 231.

[23] M.S. Namini, F. Daneshimehr, N. Beheshtizadeh, V. Mansouri, J. Ai, H.K. Jahromi, S. Ebrahimi-Barough, Cell-free therapy based on extracellular vesicles: a promising therapeutic strategy for peripheral nerve injury, Stem Cell Res. Ther. 14 (1) (2023) 254.

[24] J.B. Foo, Q.H. Looi, P.P. Chong, N.H. Hassan, G.E.C. Yeo, C.Y. Ng, B. Koh, C. W. How, S.H. Lee, J.X. Law, Comparing the therapeutic potential of stem cells and their secretory products in regenerative medicine, Stem Cell. Int. 2021 (2021) 2616807.

[25] B. Li, Y. Xing, Y. Gan, J. He, H. Hua, Labial gland-derived mesenchymal stem cells and their exosomes ameliorate murine Sjogren's syndrome by modulating the balance of Treg and Th17 cells, Stem Cell Res. Ther. 12 (1) (2021) 478.

[26] J. Zhao, Q. An, X. Zhu, B. Yang, X. Gao, Y. Niu, L. Zhang, K. Xu, D. Ma, Research status and future prospects of extracellular vesicles in primary Sjogren's syndrome, Stem Cell Res. Ther. 13 (1) (2022) 230.

[27] F. Mohajer, B. Mirhosseini-Eshkevari, S. Ahmadi, M.A. Ghasemzadeh, G.M. Ziarani, A. Badiei, N. Farshidfar, R.S. Varma, N. Rabiee, S. Iravani, Advanced nanosystems for cancer therapeutics: a review, ACS Appl. Nano Mater. 6 (9) (2023) 7123–7149.

[28] M.A. Kumar, S.K. Baba, H.Q. Sadida, S.A. Marzooqi, J. Jerobin, F.H. Altemani, N. Algehainy, M.A. Alanazi, A.B. Abou-Samra, R. Kumar, A.S.A.S. Akil, M. A. Macha, R. Mir, A.A. Bhat, Extracellular vesicles as tools and targets in therapy for diseases, Signal Transduct Tar 9 (1) (2024).

[29] M.S. Khubutiya, A.V. Vagabov, A.A. Temnov, A.N. Sklifas, Paracrine mechanisms of proliferative, anti-apoptotic and anti-inflammatory effects of mesenchymal stromal cells in models of acute organ injury, Cytotherapy 16 (5) (2014) 579–585.

[30] X. Teng, L. Chen, W. Chen, J. Yang, Z. Yang, Z. Shen, Mesenchymal stem cell-derived exosomes improve the microenvironment of infarcted myocardium contributing to angiogenesis and anti-inflammation, Cell. Physiol. Biochem. 37 (6) (2015) 2415–2424.

[31] D. Kouroupis, C. Sanjurjo-Rodriguez, E. Jones, D. Correa, Mesenchymal stem cell functionalization for enhanced therapeutic applications, Tissue Eng., Part B 25 (1) (2019) 55–77.

[32] R.W. Yeo, R.C. Lai, B. Zhang, S.S. Tan, Y. Yin, B.J. Teh, S.K. Lim, Mesenchymal stem cell: an efficient mass producer of exosomes for drug delivery, Adv. Drug Deliv. Rev. 65 (3) (2013) 336–341.

[33] Z. Weng, B. Zhang, C. Wu, F. Yu, B. Han, B. Li, L. Li, Therapeutic roles of mesenchymal stem cell-derived extracellular vesicles in cancer, J. Hematol. Oncol. 14 (1) (2021) 136.

[34] D.E. Murphy, O.G. de Jong, M. Brouwer, M.J. Wood, G. Lavieu, R.M. Schiffelers, P. Vader, Extracellular vesicle-based therapeutics: natural versus engineered targeting and trafficking, Exp. Mol. Med. 51 (3) (2019) 1–12.

[35] I.K. Herrmann, M.J.A. Wood, G. Fuhrmann, Extracellular vesicles as a next-generation drug delivery platform, Nat. Nanotechnol. 16 (7) (2021) 748–759.

[36] A. Gorgens, G. Corso, D.W. Hagey, R. Jawad Wiklander, M.O. Gustafsson, U. Felldin, Y. Lee, R.B. Bostancioglu, H. Sork, X. Liang, W. Zheng, D.K. Mohammad, S.I. van de Wakker, P. Vader, A.M. Zickler, D.R. Mamand, L. Ma, M.N. Holme, M. M. Stevens, O.P.B. Wiklander, S. El Andaloussi, Identification of storage conditions stabilizing extracellular vesicles preparations, J. Extracell. Vesicles 11 (6) (2022) e12238.

[37] M. Rahimnejad, F. Rasouli, S. Jahangiri, S. Ahmadi, N. Rabiee, M. Ramezani Farani, O. Akhavan, M. Asadnia, Y. Fatahi, S. Hong, J. Lee, J. Lee, S.K. Hahn, Engineered biomimetic membranes for organ-on-a-chip, ACS Biomater. Sci. Eng. 8 (12) (2022) 5038–5059.

[38] R. Umeda, Y. Satouh, M. Takemoto, Y. Nakada-Nakura, K. Liu, T. Yokoyama, M. Shirouzu, S. Iwata, N. Nomura, K. Sato, M. Ikawa, T. Nishizawa, O. Nureki, Structural insights into tetraspanin CD9 function, Nat. Commun. 11 (1) (2020) 1606.

[39] W. Zheng, J. Radler, H. Sork, Z. Niu, S. Roudi, J.P. Bost, A. Gorgens, Y. Zhao, D. R. Mamand, X. Liang, O.P.B. Wiklander, T. Lehto, D. Gupta, J.Z. Nordin, S. El Andaloussi, Identification of scaffold proteins for improved endogenous engineering of extracellular vesicles, Nat. Commun. 14 (1) (2023) 4734.

[40] T. Suwatthanarak, K. Ito, M. Tanaka, K. Sugiura, A. Hoshino, Y. Miyamoto, K. Miyado, M. Okochi, A peptide binding to the tetraspanin CD9 reduces cancer metastasis, Biomater. Adv. 146 (2023) 213283.

[41] H. Lazareth, C. Henique, O. Lenoir, V.G. Puelles, M. Flamant, G. Bollee, C. Fligny, M. Camus, L. Guyonnet, C. Millien, F. Gaillard, A. Chipont, B. Robin, S. Fabrega, N. Dhaun, E. Camerer, O. Kretz, F. Grahammer, F. Braun, T.B. Huber, D. Nochy, C. Mandet, P. Bruneval, L. Mesnard, E. Thervet, A. Karras, F. Le Naour, E. Rubinstein, C. Boucheix, A. Alexandrou, M.J. Moeller, C. Bouzigues, P. L. Tharaux, The tetraspanin CD9 controls migration and proliferation of parietal epithelial cells and glomerular disease progression, Nat. Commun. 10 (1) (2019) 3303.

[42] H. Mou, V. Vinarsky, P.R. Tata, K. Brazauskas, S.H. Choi, A.K. Crooke, B. Zhang, G. M. Solomon, B. Turner, H. Bihler, J. Harrington, A. Lapey, C. Channick, C. Keyes, A. Freund, S. Artandi, M. Mense, S. Rowe, J.F. Engelhardt, Y.C. Hsu, J. Rajagopal, Dual SMAD signaling inhibition enables long-term expansion of diverse epithelial basal cells, Cell Stem Cell 19 (2) (2016) 217–231.

[43] C. Zhang, H.J. Lee, A. Shrivastava, R. Wang, T.J. McQuiston, S.S. Challberg, B. A. Pollok, T. Wang, Long-term in vitro expansion of epithelial stem cells enabled by pharmacological inhibition of PAK1-ROCK-myosin II and TGF-beta signaling, Cell Rep. 25 (3) (2018) 598–610, e5.

[44] C. Théry, K.W. Witwer, E. Aikawa, M.J. Alcaraz, J.D. Anderson, R. Andriantsitohaina, A. Antoniou, T. Arab, F. Archer, G.K. Atkin-Smith, D.C. Ayre, J.M. Bach, D. Bachurski, H. Baharvand, L. Balaj, S. Baldacchino, N.N. Bauer, A. A. Baxter, M. Bebawy, C. Beckham, A.B. Zavec, A. Benmoussa, A.C. Berardi, P. Bergese, E. Bielska, C. Blenkiron, S. Bobis-Wozowicz, E. Boilard, W. Boireau, A. Bongiovanni, F.E. Borràs, S. Bosch, C.M. Boulanger, X. Breakefield, A.M. Breglio, M.A. Brennan, D.R. Brigstock, A. Brisson, M.L.D. Broekman, J.F. Bromberg, P. Bryl-Górecka, S. Buch, A.H. Buck, D. Burger, S. Busatto, D. Buschmann, B. Bussolati, E. I. Buzas, J.B. Byrd, G. Camussi, D.R.F. Carter, S. Caruso, L.W. Chamley, Y.T. Chang, C.C. Chen, S. Chen, L. Cheng, A.R. Chin, A. Clayton, S.P. Clerici, A. Cocks, E. Cocucci, R.J. Coffey, A. Cordeiro-da-Silva, Y. Couch, F.A.W. Coumans, B. Coyle, R. Crescitelli, M.F. Criado, C. D'Souza-Schorey, S. Das, A.D. Chaudhuri, P. de Candia, E.F. De Santana, O. De Wever, H.A. del Portillo, T. Demaret, S. Deville, A. Devitt, B. Dhondt, D. Di Vizio, L.C. Dieterich, V. Dolo, A.P.D. Rubio, M. Dominici, M.R. Dourado, T.A.P. Driedonks, F.V. Duarte, H.M. Duncan, R. M. Eichenberger, K. Ekström, S.E.L. Andaloussi, C. Elie-Caille, U. Erdbrügger, J. M. Falcón-Pérez, F. Fatima, J.E. Fish, M. Flores-Bellver, A. Försönits, A. Frelet-Barrand, F. Fricke, G. Fuhrmann, S. Gabrielsson, A. Gámez-Valero, C. Gardiner, K. Gärtner, R. Gaudin, Y.S. Gho, B. Giebel, C. Gilbert, M. Gimona, I. Giusti, D.C. I. Goberdhan, A. Görgens, S.M. Gorski, D.W. Greening, J.C. Gross, A. Gualerzi, G. N. Gupta, D. Gustafson, A. Handberg, R.A. Haraszti, P. Harrison, H. Hegyesi, A. Hendrix, A.F. Hill, F.H. Hochberg, K.F. Hoffmann, B. Holder, H. Holthofer, B. Hosseinkhani, G.K. Hu, Y.Y. Huang, V. Huber, S. Hunt, A.G.E. Ibrahim, T. Ikezu, J.M. Inal, M. Isin, A. Ivanova, H.K. Jackson, S. Jacobsen, S.M. Jay, M. Jayachandran, G. Jenster, L.Z. Jiang, S.M. Johnson, J.C. Jones, A. Jong, T. Jovanovic-Talisman, S. Jung, R. Kalluri, S. Kano, S. Kaur, Y. Kawamura, E. T. Keller, D. Khamari, E. Khomyakova, A. Khvorova, P. Kierulf, K.P. Kim, T. Kislinger, M. Klingeborn, D.J. Klinke, M. Kornek, M.M. Kosanovic, A.F. Kovács, E.M. Krämer-Albers, S. Krasemann, M. Krause, I.V. Kurochkin, G.D. Kusuma, S. Kuypers, S. Laitinen, S.M. Langevin, L.R. Languino, J. Lannigan, C. Lässer, L. C. Laurent, G. Lavieu, E. Lázaro-Ibáñez, S. Le Lay, M.S. Lee, Y.X.F. Lee, D.S. Lemos, M. Lenassi, A. Leszczynska, I.T.S. Li, K. Liao, S.F. Libregts, E. Ligeti, R. Lim, S. K. Lim, A. Line, K. Linnemannstöns, A. Llorente, C.A. Lombard, M.J. Lorenowicz, A. M. Lörincz, J. Lötvall, J. Lovett, M.C. Lowry, X. Loyer, Q. Lu, B. Lukomska, T. R. Lunavat, S.L.N. Maas, H. Malhi, A. Marcilla, J. Mariani, J. Mariscal, E. S. Martens-Uzunova, L. Martin-Jaular, M.C. Martinez, V.R. Martins, M. Mathieu, S. Mathivanan, M. Maugeri, L.K. McGinnis, M.J. McVey, D.G. Meckes, K.L. Meehan, I. Mertens, V.R. Minciacchi, A. Möller, M.M. Jorgensen, A. Morales-Kastresana, J. Morhayim, F. Mullier, M. Muraca, L. Musante, V. Mussack, D.C. Muth, K. H. Myburgh, T. Najrana, M. Nawaz, I. Nazarenko, P. Nejsum, C. Neri, T. Neri, R. Nieuwland, L. Nimrichter, J.P. Nolan, E.N.M. Nolte-'t Hoen, N. Noren Hooten, L. O'Driscoll, T. O'Grady, A. O'Loghlen, T. Ochiya, M. Olivier, A. Ortiz, L.A. Ortiz, X. Osteikoetxea, O. Ostegaard, M. Ostrowski, J. Park, D.M. Pegtel, H. Peinado, F. Perut, M.W. Pfaffl, D.G. Phinney, B.C.H. Pieters, R.C. Pink, D.S. Pisetsky, E. P. von Strandmann, I. Polakovicova, I.K.H. Poon, B.H. Powell, I. Prada, L. Pulliam, P. Quesenberry, A. Radeghieri, R.L. Raffai, S. Raimondo, J. Rak, M.I. Ramirez, G. Raposo, M.S. Rayyan, N. Regev-Rudzki, F.L. Ricklefs, P.D. Robbins, D. D. Roberts, S.C. Rodrigues, E. Rohde, S. Rome, K.M.A. Rouschop, A. Rughetti, A. E. Russell, P. Saá, S. Sahoo, E. Salas-Huenuleo, C. Sánchez, J.A. Saugstad, M. J. Saul, R.M. Schiffelers, R. Schneider, T.H. Schoyen, A. Scott, E. Shahaj, S. Sharma, O. Shatnyeva, F. Shekari, G.V. Shelke, A.K. Shetty, K. Shiba, P.R.M. Siljander, A. M. Silva, A. Skowronek, O.L. Snyder, R.P. Soares, B.W. Sódar, C. Soekmadji, J. Sotillo, P.D. Stahl, W. Stoorvogel, S.L. Stott, E.F. Strasser, S. Swift, H. Tahara, M. Tewari, K. Timms, S. Tiwari, R. Tixeira, M. Tkach, W.S. Toh, R. Tomasini, A. C. Torrecilhas, J.P. Tosar, V. Toxavidis, L. Urbanelli, P. Vader, B.W.M. van Balkom, S.G. van der Grein, J. Van Deun, M.J.C. van Herwijnen, K. Van Keuren-Jensen, G. van Niel, M.E. van Royen, A.J. van Wijnen, M.H. Vasconcelos, I.J. Vechetti, T. D. Veit, L.J. Vella, É. Velot, F.J. Verweij, B. Vestad, J.L. Viñas, T. Visnovitz, K. V. Vukman, J. Wahlgren, D.C. Watson, M.H.M. Wauben, A. Weaver, J.P. Webber, V. Weber, A.M. Wehman, D.J. Weiss, J.A. Welsh, S. Wendt, A.M. Wheelock, Z. Wiener, L. Witte, J. Wolfram, A. Xagorari, P. Xander, J. Xu, X.M. Yan, M. Yáñez-Mó, H. Yin, Y. Yuana, V. Zappulli, J. Zarubova, V. Zekas, J.Y. Zhang, Z.Z. Zhao, L. Zheng, A.R. Zheutlin, A.M. Zickler, P. Zimmermann, A.M. Zivkovic, D. Zocco, E. K. Zuba-Surma, Minimal information for studies of extracellular vesicles 2018 (MISEV2018): a position statement of the International Society for Extracellular Vesicles and update of the MISEV2014 guidelines, J. Extracell. Vesicles 7 (1) (2018).

[45] H. Gwak, S. Park, J. Kim, J.D. Lee, I.S. Kim, S.I. Kim, K.A. Hyun, H.I. Jung, Microfluidic chip for rapid and selective isolation of tumor-derived extracellular vesicles for early diagnosis and metastatic risk evaluation of breast cancer, Biosens. Bioelectron. 192 (2021).

[46] H. Gwak, S. Park, H. Yu, K.A. Hyun, H.I. Jung, A modular microfluidic platform for serial enrichment and harvest of pure extracellular vesicles, Analyst 147 (6) (2022) 1117–1127.

[47] H. Yu, J. Kim, J. Yu, K.A. Hyun, J.Y. Lim, Y.J. Yoon, S. Park, H.I. Jung, Continuous isolation of stem-cell-derived extracellular vesicles (SC-EVs) by recycled magnetic beads in microfluidic channels, Biochip J (2023).

[48] J.M. Cho, Y.J. Yoon, S. Lee, D. Kim, D. Choi, J. Kim, J.Y. Lim, Retroductal delivery of epidermal growth factor protects salivary progenitors after irradiation, J. Dent. Res. 100 (8) (2021) 883–890.

[49] D. Kim, K.M. Lim, J.M. Cho, H.J. Park, S. Hwang, A.A. Dayem, Y.J. Jeong, Y. Shin, Y. Hong, K. Song, S.G. Cho, J.Y. Lim, Ductal delivery of extracellular vesicles promote the recovery from salivary gland inflammation, J. Contr. Release 357 (2023) 235–248.

[50] S. Hwang, J.M. Cho, Y.J. Yoon, S. Seo, Y. Hong, J.Y. Lim, Retroductal dexamethasone administration promotes the recovery from obstructive and inflammatory salivary gland dysfunction, Front. Immunol. 15 (2024) 1418703.

[51] Y.J. Yoon, D. Kim, K.Y. Tak, S. Hwang, J. Kim, N.S. Sim, J.M. Cho, D. Choi, Y. Ji, J. K. Hur, H. Kim, J.E. Park, J.Y. Lim, Salivary gland organoid culture maintains distinct glandular properties of murine and human major salivary glands, Nat. Commun. 13 (1) (2022) 3291.

[52] Y. Kuriki, Y. Liu, D. Xia, E.M. Gjerde, S. Khalili, B. Mui, C. Zheng, S.D. Tran, Cannulation of the mouse submandibular salivary gland via the Wharton's duct, J. Vis. Exp. 51 (2011).

[53] B.D. Noll, A. Grdzelishvili, M.T. Brennan, F.B. Mougeot, J.C. Mougeot, Immortalization of salivary gland epithelial cells of xerostomic patients: establishment and characterization of novel cell lines, J. Clin. Med. 9 (12) (2020).

[54] T. Yi, S. Lee, N. Choi, H.S. Shin, J. Kim, J.Y. Lim, Single cell clones purified from human parotid glands display features of multipotent epitheliomesenchymal stem cells, Sci. Rep. 6 (2016) 36303.

[55] H. Nam, J.H. Kim, J.Y. Hwang, G.H. Kim, J.W. Kim, M. Jang, J.H. Lee, K. Park, G. Lee, Characterization of primary epithelial cells derived from human salivary gland contributing to in vivo formation of acini-like structures, Mol. Cell. 41 (6) (2018) 515–522.

[56] E.I. Buzás, E.A. Tóth, B.W. Sódar, K.É. Szabó-Taylor, Molecular interactions at the surface of extracellular vesicles, Semin. Immunopathol. 40 (5) (2018) 453–464.

[57] Y. Zhang, Y.F. Liu, H.Y. Liu, W.H. Tang, Exosomes: biogenesis, biologic function and clinical potential, Cell Biosci. 9 (2019).

[58] M.W. Kim, S. Park, H. Lee, H. Gwak, K.A. Hyun, J.Y. Kim, H.I. Jung, S.I. Kim, Multi-miRNA panel of tumor-derived extracellular vesicles as promising diagnostic biomarkers of early-stage breast cancer, Cancer Sci. 112 (12) (2021) 5078–5087.

[59] D. Wlodkowic, W. Telford, J. Skommer, Z. Darzynkiewicz, Apoptosis and beyond: cytometry in studies of programmed cell death, Methods Cell Biol. 103 (2011) 55–98.

[60] F.M. Barros, F. Carneiro, J.C. Machado, S.A. Melo, Exosomes and immune response in cancer: friends or foes? Front. Immunol. 9 (2018) 730.

[61] Y. Chen, G. Li, M.L. Liu, Microvesicles as emerging biomarkers and therapeutic targets in cardiometabolic diseases, Dev. Reprod. Biol. 16 (1) (2018) 50–62.

[62] L. Console, M. Scalise, C. Indiveri, Exosomes in inflammation and role as biomarkers, Clin. Chim. Acta 488 (2019) 165–171.

[63] Y. Fan, C. Pionneau, F. Cocozza, P.Y. Boëlle, S. Chardonnet, S. Charrin, C. Thery, P. Zimmermann, E. Rubinstein, Differential proteomics argues against a general role for CD9, CD81 or CD63 in the sorting of proteins into extracellular vesicles, J. Extracell. Vesicles 12 (8) (2023).

[64] K. Chen, Y. Li, L.W. Xu, Y.G. Qian, N. Liu, C.C. Zhou, J.Y. Liu, L.H. Zhou, Z. Xu, R. P. Jia, Y.Z. Ge, Comprehensive insight into endothelial progenitor cell-derived extracellular vesicles as a promising candidate for disease treatment, Stem Cell Res. Ther. 13 (1) (2022).

[65] G.H. Lou, Z. Chen, M. Zheng, Y.N. Liu, Mesenchymal stem cell-derived exosomes as a new therapeutic strategy for liver diseases, Exp. Mol. Med. 49 (2017).

[66] S. Nikfarjam, J. Rezaie, N.M. Zolbanin, R. Jafari, Mesenchymal stem cell derived-exosomes: a modern approach in translational medicine, J. Transl. Med. 18 (1) (2020).

[67] F. Tan, X.R. Li, Z. Wang, J.J. Li, K. Shahzad, J.L. Zheng, Clinical applications of stem cell-derived exosomes, Signal Transduct Tar 9 (1) (2024).

[68] R. Kalluri, V.S. LeBleu, The biology, function, and biomedical applications of exosomes, Science 367 (6478) (2020) 640.

[69] Y.Y. Tang, Y. Zhou, H.J. Li, Advances in mesenchymal stem cell exosomes: a review, Stem Cell Res. Ther. 12 (1) (2021).

[70] J.J. Lai, Z.L. Chau, S.Y. Chen, J.J. Hill, K.V. Korpany, N.W. Liang, L.H. Lin, Y. H. Lin, J.K. Liu, Y.C. Liu, R. Lunde, W.T. Shen, Exosome processing and characterization approaches for research and technology development, Adv. Sci. 9 (15) (2022) e2103222.

[71] J. Wang, E.E. Bonacquisti, A.D. Brown, J. Nguyen, Boosting the biogenesis and secretion of mesenchymal stem cell-derived exosomes, Cells 9 (3) (2020).

[72] T.C. Jiang, Z.Y. Wang, J. Sun, Human bone marrow mesenchymal stem cell-derived exosomes stimulate cutaneous wound healing mediates through TGF-β/Smad signaling pathway, Stem Cell Res. Ther. 11 (1) (2020).

[73] Y.Y. Han, J.X. Yang, J.K. Fang, Y.P. Zhou, E. Candi, J.H. Wang, D. Hua, C.S. Shao, Y.F. Shi, The secretion profile of mesenchymal stem cells and potential applications in treating human diseases, Signal Transduct Tar 7 (1) (2022).

[74] K.M. Lim, S. Kim, J. Yeom, Y. Choi, Y. Lee, J. An, M. Gil, A.A. Dayem, K. Kim, G. H. Kang, A. Kim, K. Hong, K. Kim, S.G. Cho, Advanced 3D dynamic culture system with transforming growth factor-B3 enhances production of potent extracellular

vesicles with modified protein cargoes via upregulation of TGF-B signaling, J. Adv. Res. 47 (2023) 57–74.

[75] M. Mathieu, L. Martin-Jaular, G. Lavieu, C. Théry, Specificities of secretion and uptake of exosomes and other extracellular vesicles for cell-to-cell communication, Nat. Cell Biol. 21 (1) (2019) 9–17.

[76] M. Mathieu, N. Névo, M. Jouve, J.I. Valenzuela, M. Maurin, F.J. Verweij, R. Palmulli, D. Lankar, F. Dingli, D. Loew, E. Rubinstein, G. Boncompain, F. Perez, C. Théry, Specificities of exosome versus small ectosome secretion revealed by live intracellular tracking of CD63 and CD9, Nat. Commun. 12 (1) (2021).

[77] J. Nigri, J. Leca, S.S. Tubiana, P. Finetti, F. Guillaumond, S. Martinez, S. Lac, J. L. Iovanna, S. Audebert, L. Camoin, S. Vasseur, F. Bertucci, R. Tomasini, CD9 mediates the uptake of extracellular vesicles from cancer-associated fibroblasts that promote pancreatic cancer cell aggressiveness, Sci. Signal. 15 (745) (2022).

[78] W.M. Longmate, C.M. Dipersio, Integrin regulation of epidermal functions in wounds, Adv. Wound Care 3 (3) (2014) 229–246.

[79] X.C. Pang, X. He, Z.W. Qiu, H.X. Zhang, R. Xie, Z.Y. Liu, Y.L. Gu, N. Zhao, Q. Xiang, Y.M. Cui, Targeting integrin pathways: mechanisms and advances in therapy, Signal Transduct Tar 8 (1) (2023).

[80] F.N.A. Jahromi, R. Dowran, R. Jafari, Recent advances in the roles of exosomal microRNAs (exomiRs) in hematologic neoplasms: pathogenesis, diagnosis, and treatment, Cell Commun. Signal. 21 (1) (2023).

[81] E. Oveili, S. Vafaei, H. Bazavar, Y. Eslami, E. Mamaghanizadeh, S. Yasamineh, O. Gholizadeh, The potential use of mesenchymal stem cells-derived exosomes as microRNAs delivery systems in different diseases, Cell Commun. Signal. 21 (1) (2023).

[82] X.M. Meng, D.J. Nikolic-Paterson, H.Y. Lan, Tgf-β: the master regulator of fibrosis, Nat. Rev. Nephrol. 12 (6) (2016) 325–338.

[83] Y. Tai, C. Zhao, J. Gao, T. Lan, H. Tong, Identification of miRNA-target gene regulatory networks in liver fibrosis based on bioinformatics analysis, PeerJ 9 (2021) e11910.

[84] K. Usman, A. Hsieh, T.L. Hackett, The role of miRNAs in extracellular matrix repair and chronic fibrotic lung diseases, Cells 10 (7) (2021).

[85] D.M. Adyshev, N. Moldobaeva, B. Mapes, V. Elangovan, J.G. Garcia, MicroRNA regulation of nonmuscle myosin light chain kinase expression in human lung endothelium, Am. J. Respir. Cell Mol. Biol. 49 (1) (2013) 58–66.

[86] D. Chickooree, K. Zhu, V. Ram, H.J. Wu, Z.J. He, S. Zhang, A preliminary microarray assay of the miRNA expression signatures in buccal mucosa of oral submucous fibrosis patients, J. Oral Pathol. Med. 45 (9) (2016) 691–697.

[87] Y. Huang, L. Chen, Z. Feng, W. Chen, S. Yan, R. Yang, J. Xiao, J. Gao, D. Zhang, X. Ke, EPC-derived exosomal miR-1246 and miR-1290 regulate phenotypic changes of fibroblasts to endothelial cells to exert protective effects on myocardial infarction by targeting ELF5 and SP1, Front. Cell Dev. Biol. 9 (2021) 647763.

[88] J. Song, B. Song, L. Yuan, G. Yang, Multiplexed strategies toward clinical translation of extracellular vesicles, Theranostics 12 (15) (2022) 6740–6761.